

University of Nebraska - Lincoln

DigitalCommons@University of Nebraska - Lincoln

Civil Engineering Theses, Dissertations, and
Student Research

Civil Engineering


Fall 12-2011

Sensitivity Analysis on Mapping EvapoTranspiration at High Resolution Using Internal Calibration (METRIC)

Venkata Naga Ravi Kumar Choragudi

University of Nebraska-Lincoln, ravikumarch2003@gmail.com

Follow this and additional works at: <https://digitalcommons.unl.edu/civilengdiss>

 Part of the [Agricultural and Resource Economics Commons](#), [Civil Engineering Commons](#), [Environmental Engineering Commons](#), [Geographic Information Sciences Commons](#), and the [Other Civil and Environmental Engineering Commons](#)

Choragudi, Venkata Naga Ravi Kumar, "Sensitivity Analysis on Mapping EvapoTranspiration at High Resolution Using Internal Calibration (METRIC)" (2011). *Civil Engineering Theses, Dissertations, and Student Research*. 35.

<https://digitalcommons.unl.edu/civilengdiss/35>

This Article is brought to you for free and open access by the Civil Engineering at DigitalCommons@University of Nebraska - Lincoln. It has been accepted for inclusion in Civil Engineering Theses, Dissertations, and Student Research by an authorized administrator of DigitalCommons@University of Nebraska - Lincoln.

SENSITIVITY ANALYSIS ON MAPPING EVAPOTRANSPIRATION AT HIGH
RESOLUTION USING INTERNAL CALIBRATION (METRIC)

by

Ravi Choragudi

A THESIS

Presented to the Faculty of

The Graduate College at the University of Nebraska

In Partial Fulfillment of Requirements

For the Degree of Master of Science

Major: Civil Engineering

Under the Supervision of Professor Ayse Irmak

Lincoln, Nebraska

August, 2011

SENSITIVITY ANALYSIS ON MAPPING EVAPOTRANSPIRATION AT HIGH RESOLUTION USING INTERNAL CALIBRATION (METRIC)

Ravi Choragudi, M.S.

University of Nebraska, 2011

Adviser: Ayse Irmak

Mapping EvapoTranspiration at high Resolution using Internal Calibration (METRIC) is most widely used to quantify evapotranspiration (ET) spatially and temporally. It is essential to inspect the model's response to errors in various parameters used in the model. Landsat 5 images from May 30 2009, July 1 2009 and a Landsat 7 image from September 27 2009 are used in this study. Fourteen different fields composed of Corn, Soybeans, Alfalfa are randomly chosen for each crop type.

Two kinds of errors are addressed in this study. One, with the errors that are transferred and potentially compensated by calibration (Global error) and the other is the error that is not passed into the calibration (Local error). For global error, Reflectance at the satellite (ρ), transmissivity (τ), surface temperature (T_s), wind speed (u), Reference Evapotranspiration (ET_r) are chosen. In addition, the sensitivity towards selection of hot and cold pixels is also investigated. For local errors, albedo (α), surface temperature (T_s), momentum roughness length (Z_{om}), soil heat flux (G), difference between air and surface temperature (dT) are considered.

In this study, we have found that METRIC is able to compensate most of the global errors passed through the calibration to give consistent results, when the variables considered above has changed to their extremes. ET_r should be estimated at a good

degree of accuracy to maintain the METRIC's results to be realistic. Also, selection of hot and cold pixels is the most crucial and sensitive process in METRIC.

In case of local errors: Z_{om} is relatively insensitive to the model. dT is found to be the most sensitive variable for bare soils. However, the other parameters are linearly proportional to their errors.

Acknowledgements

I would like to thank several people for their help and co-operation extended for completion of this endeavor.

First, I would like to sincerely thank my brother in law Dr. Vamsi Krishna Palukuru for encouraging me to do research, without whom my graduate studies could not have been possible. Also, my beloved sister Aruna and brother Aditya Choragudi took my responsibilities on their shoulders to drive towards successful completion of my graduate studies. I thank for their continuous help and support extended me from all directions. I would like to appreciate my Nephew cutie Ritwik Palukuru, for helping his share to keep me out of pressure during my research program. I would like to thank my mom; Kusuma Kumari Choragudi for supporting my studies right from childhood and helping me getting out of the tough situations, provided me love, moral and economic support.

My friends Krishna swamy Nallamreddy, Bharath Reddy Annapareddy, Rama Krishna Thummalapalli, Vijaya Krishna Musunuru have provided me all facilities financially, morally, and technically. Their support is priceless and no words can describe their friendship and affection. I also would like to thank my roommates, Shashank Reddy Gajjala, Wajid Abdul Mohammed, for providing me ideal conditions for my studies and being patient with me and understanding my difficulties during peak times.

I would like to thank my fellow HIS members: Babu Rao Kamble, for introducing me this area of interest and continuous guidance, Nathan Healey: for sharing his thoughts, helping me as a fellow teaching assistant and helping me in my problems due to

cultural differences. Also, Ian Ratcliffe, who helped me technically without any hesitation irrespective of his busy schedules. I would also like to appreciate Osama Z Akasheh for his support at elementary levels.

I would most like to thank Dr. Ayse Irmak who is responsible for this research study for funding and motivating me. I sincerely thank Dr. Richard Allen for his valuable suggestions and insights and critics on my work. I would also like to thank Dr. Kenneth Hubbard and Dr. Xu Li for accepting to be as my committee members and feedback they provided.

I wanted to thank SNR faculty and staff who directly or indirectly helped me and addressed my problems.

Table of Contents

Chapter 1: Introduction	1
Chapter 2: Materials and Methods	5
2.1 METRIC	5
2.2 Weather station and site conditions	12
Chapter 3: Global Error	16
3.1 Methodology	16
3.2 Results and Discussion	17
3.2.1 Reflectance at satellite (ρ).....	17
3.2.2 Transmittance error (τ).....	21
3.2.3 Surface Temperature (T_s).....	26
3.2.4 Reference Evapotranspiration and wind speed (ET_r & u).....	29
3.2.5 Sensitivity towards Selecting Hot and Cold Pixels.....	38
Chapter 4: Local error	44
4.1 Methodology	44
4.2 Results and Discussions	45
4.2.1 Albedo (α).....	45
4.2.2 Soil heat flux (G)	49
4.2.3 Momentum roughness length Z_{om}	54
4.2.4 Near surface temperature difference dT	57
4.2.5 Surface temperature T_s	61
Chapter 5: Conclusions	65
References.....	68
Appendix A:.....	78

List of Figures

FIGURE 1: WEATHER STATION LOCATION	13
FIGURE 2: SENSITIVITY TO REFLECTANCE ON MAY 30 2009	19
FIGURE 3: SENSITIVITY TO REFLECTANCE ON JULY 1 2009	20
FIGURE 4: SENSITIVITY TO REFLECTANCE ON SEPTEMBER 27 2009.....	20
FIGURE 5: SENSITIVITY TO TRANSMITTANCE ON MAY 30 2009	23
FIGURE 6: SENSITIVITY TO TRANSMITTANCE ON JULY 1 2009	23
FIGURE 7: SENSITIVITY TO TRANSMITTANCE ON SEPTEMBER 27 2009.....	24
FIGURE 8: SENSITIVITY OF MODEL TO T_s AT GLOBAL SCALE, ON MAY 30 2009	27
FIGURE 9: SENSITIVITY OF MODEL TO T_s AT GLOBAL SCALE, ON JULY 1 2009	27
FIGURE 10: SENSITIVITY OF MODEL TO T_s AT GLOBAL SCALE, ON SEPTEMBER 27 2009	28
FIGURE 11: IMPACT OF WIND SPEED VARIATIONS ON THE MODEL FOR MAY 30 2009	30
FIGURE 12: IMPACT OF WIND SPEED VARIATIONS ON THE MODEL FOR JULY 1 2009	30
FIGURE 13: IMPACT OF WIND SPEED VARIATIONS ON THE MODEL FOR SEPTEMBER 27 2009 IMAGE	31
FIGURE 14: MODEL SENSITIVITY TO REFERENCE EVAPOTRANSPIRATION ON MAY 30 2009	32
FIGURE 15: MODEL SENSITIVITY TO REFERENCE EVAPOTRANSPIRATION ON JULY 1 2009	33
FIGURE 16: MODEL SENSITIVITY TO REFERENCE EVAPOTRANSPIRATION ON SEPTEMBER 27 2009	33
FIGURE 17: INSTANTANEOUS ET VARIATIONS FOR MAY 30 2009 IMAGE	34
FIGURE 18: INSTANTANEOUS ET VARIATIONS FOR JULY 1 2009 IMAGE	35
FIGURE 19: INSTANTANEOUS ET VARIATIONS FOR SEPTEMBER 27 2009 IMAGE	36
FIGURE 20: : SENSITIVITY OF THE MODEL TO SELECTION OF COLD PIXELS ON MAY 30 2009.....	39
FIGURE 21: SENSITIVITY OF THE MODEL TO SELECTION OF COLD PIXELS ON JULY 1 2009.....	39
FIGURE 22: SENSITIVITY OF THE MODEL TO SELECTION OF COLD PIXELS ON SEPTEMBER 27 2009	40
FIGURE 23: SENSITIVITY OF THE MODEL TO SELECTION OF HOT PIXELS FOR MAY 30 2009	41
FIGURE 24: SENSITIVITY OF THE MODEL TO SELECTION OF HOT PIXELS FOR JULY 1 2009	41
FIGURE 25: SENSITIVITY OF THE MODEL TO SELECTION OF HOT PIXELS FOR SEPTEMBER 27 2009.....	42
FIGURE 26: METRIC'S LOCAL SENSITIVITY TO ALBEDO FOR MAY IMAGE	47
FIGURE 27: METRIC'S LOCAL SENSITIVITY TO ALBEDO FOR JULY IMAGE	47
FIGURE 28: METRIC'S LOCAL SENSITIVITY TO ALBEDO FOR SEPTEMBER IMAGE.....	48
FIGURE 29: MODEL RESPONSE TO VARIATIONS IN G FOR MAY IMAGE	51
FIGURE 30: MODEL RESPONSE TO VARIATIONS IN G FOR JULY IMAGE	51
FIGURE 31: MODEL RESPONSE TO VARIATIONS IN G FOR SEPTEMBER IMAGE.....	52
FIGURE 32: CHANGE IN ET WITH VARIATIONS IN Z_{OM} FOR MAY IMAGE.....	55
FIGURE 33: CHANGE IN ET WITH VARIATIONS IN Z_{OM} FOR JULY IMAGE.....	55
FIGURE 34: CHANGE IN ET WITH VARIATIONS IN Z_{OM} FOR SEPTEMBER IMAGE	56
FIGURE 35: CHANGES IN ET_{rF} WITH ERROR IN dT FOR MAY IMAGE	58
FIGURE 36: CHANGES IN ET_{rF} WITH ERROR IN dT FOR JULY IMAGE	58
FIGURE 37: CHANGES IN ET_{rF} WITH ERROR IN dT SEPTEMBER IMAGE	59
FIGURE 38: MODEL'S RESPONSE TO CHANGE IN LOCAL T_s FOR MAY IMAGE	62
FIGURE 39: MODEL'S RESPONSE TO CHANGE IN LOCAL T_s FOR JULY IMAGE	62
FIGURE 40: MODEL'S RESPONSE TO CHANGE IN LOCAL T_s FOR SEPTEMBER IMAGE.....	63
FIGURE A.1: VARIATIONS IN A,B WITH CHANGE IN TRANSMISSIVITY FOR MAY IMAGE	78
FIGURE A.2: VARIATIONS IN A,B WITH CHANGE IN ET_r FOR MAY IMAGE	78

LIST OF TABLES

TABLE 1: SITE CONDITIONS AND BASE VALUES OF DIFFERENT PARAMETERS, FOR THREE DIFFERENT IMAGES. MIN, MAX, AVG REPRESENT MINIMUM, MAXIMUM, AVERAGE OF FOURTEEN SELECTED FIELDS FOR EACH CROP TYPE.	15
TABLE 2: ABSOLUTE AND PERCENTAGE CHANGE IN RADIANCE AND REFLECTANCE FOR 1 DN CHANGE IN RANDOMLY SELECTED COLD AND HOT PIXELS FOR LANDSAT 5.	18
TABLE 3: ABSOLUTE CHANGE IN AVERAGE ETrF WHEN REFLECTANCE IS CHANGED, FOR ALL IMAGES CONSIDERED.	21
TABLE 4: ABSOLUTE CHANGE IN AVERAGE ETrF WHEN TRANSMISSIVITY IS CHANGED, FOR ALL IMAGES CONSIDERED.	25
TABLE 5: ABSOLUTE CHANGE IN AVERAGE ETrF WHEN SURFACE TEMPERATURE IS CHANGED, FOR ALL IMAGES CONSIDERED.	29
TABLE 6: ABSOLUTE CHANGE IN AVERAGE ETrF WHEN WIND SPEED IS CHANGED, FOR ALL IMAGES CONSIDERED.	32
TABLE 7: ABSOLUTE CHANGE IN AVERAGE ETrF WHEN REFERENCE ET IS CHANGED, FOR ALL IMAGES CONSIDERED.	37
TABLE 8: MAXIMUM RELATIVE CHANGE IN ETrF, WHEN DIFFERENT HOT AND COLD PIXEL TEMPERATURES ARE SELECTED.	43
TABLE 9: MAXIMUM ABSOLUTE CHANGE IN AVERAGE ETrF WHEN ALBEDO IS CHANGED.	48
TABLE 10: MAXIMUM ABSOLUTE CHANGE IN AVERAGE ETrF WHEN SOIL HEAT FLUX IS CHANGED.	52
TABLE 11: MAXIMUM ABSOLUTE CHANGE IN AVERAGE ETrF WHEN MOMENTUM ROUGHNESS LENGTH IS CHANGED.	57
TABLE 12: MAXIMUM ABSOLUTE CHANGE IN AVERAGE ETrF WHEN DT IS CHANGED.	61
TABLE 13: MAXIMUM ABSOLUTE CHANGE IN AVERAGE ETrF WHEN SURFACE TEMPERATURE IS CHANGED AT LOCAL SCALE.	64
TABLE 14: PERCENTAGE CHANGE IN ET_rF WHEN EACH PARAMETER IS CHANGED TO ITS EXTREME LIMIT ON ONE SIDE FOR MAY, JULY, SEPTEMBER IMAGES: GLOBAL ERROR.	65
TABLE 15: PERCENTAGE CHANGE IN ETrF WHEN EACH PARAMETER IS CHANGED TO ITS EXTREME LIMIT ON ONE SIDE FOR MAY, JULY, SEPTEMBER IMAGES: LOCAL ERROR.	67

Chapter 1: Introduction

Accurate estimation of evapotranspiration (ET) is key to various hydrological, ecological and agricultural processes. Most of the field measurements like lysimeters, Bowen ratio and Eddy covariance techniques are limited to one point and they lack the spatial distribution of ET. To overcome this problem, remote sensing (RS) is used to estimate spatial and temporal trends of ET using energy balance.

Various models are developed to quantify ET distribution using remotely sensed satellite data (Gowda et al. 2007). Land surface temperature data is not always feasible to obtain, which is the main input for most of the models. Surface Energy Balance Algorithm (SEBAL) developed by Bastiaanssen et al. (1998) concept of selecting hot and cold pixels and calibration of the model makes the process of computation of difference in temperature between surface and air (dT) simple by avoiding the need of accurate land temperature data.

Mapping Evapotranspiration with internalized calibration (METRIC) developed by Allen et al. (2007a&b) is the successor of SEBAL with few changes (Gowda et al. 2007). METRIC uses quality weather station data (air temperature, wind speed, solar radiation, relative humidity) and satellite radiance data at various bands as inputs for this model. The detailed discussion about METRIC is discussed in next section.

Santos et al. (2007) found that METRIC is useful in estimating ET for irrigation efficiency error within 3% for more than 60% of the fields used for study. Tang et al. (2009) found METRIC instantaneous ET estimates have just 10% error in estimating and

15% error in estimating daily ET. However, they also concluded that seasonal estimates from METRIC ET is overestimated compared to that of flux measurements. Case studies done by Allen et.al. (2007b) concluded that METRIC is useful in estimating ET for different types of crops in different seasons with error average about 10%.

Sensitivity analysis done by Bailey and Davies (1981) on aerodynamic resistance r_a to ET on a soybean crop field using a custom developed energy balance model resulted that the model is insensitive to r_a . But r_a is more sensitive to surface roughness than to the zero plane displacement calculated empirically from leaf area index LAI, crop height.

Gellens-Meulenberghs (2004) did sensitivity analysis on Radiation Energy Balance Systems (REBS) model for sensible heat flux H, Latent heat flux LE, varying stability functions (Hogstrom 1988, Brutsaert 1999, Brutsaert 1982, Grachev et al. 2000) and input data (Net radiation R_n , Soil heat flux G obtained empirically, Air temperature T_a , Wind speed U). This study concluded that the stability functions are sensitive to low wind speed and high temperature because at low wind speeds, the mechanical mixing component is less than the buoyancy component. Bias in temperature and wind speed enhanced rms of LE and H. Minor deviations in input data mentioned above resulted significant rms values in LE and H.

In addition to the above mentioned sensitivity analyses, Stricker and Brutsaert (1978), Goutorbe (1991) conducted sensitivity analyses, but they are limited to ground based energy algorithm.

Crow and Kustas (2005) did a sensitivity analysis on two source model (TSM) considering dT , evaporative fraction (EF), aerodynamic resistance (r_{ah}) for different

vegetative fractions from 50% to 90% (grass, pasture and shrub lands). This study revealed that the model's EF is not sensitive to vegetative fraction, but dT and rah are sensitive to vegetative fraction when radiometric surface temperature is estimated using different observation look angle and LAI. Results of sensitivity analysis on sensible heat flux (H) by Van der Kwast et al. (2009) in SEBS (Surface energy balance system) model, confirmed that H is not sensitive to Digital elevation model (DEM), Surface Emissivity, NDVI, albedo, relative humidity, height of planetary boundary layer. However, this study also confirmed that incoming short wave radiation is not sensitive to most of the cases, but only in few cases, it is sensitive in calculating H . The factors that are sensitive in calculation of H , are wind speed, air temperature, and air pressure in SEBS. Parameters obtained from fields and literature found to be sensitive to surface roughness for momentum transport, but not to the zero plane displacement and canopy height in calculation of H .

Sensitivity analysis done by Tasumi (2003) on an early version of METRIC confirmed that doubling or halving the surface roughness parameter did not change ET estimates by more than 5% for irrigated agricultural area when incorporated into the calibration. Wang et al. (2009) did a comprehensive sensitivity analysis on SEBAL for Pecan Orchards at full canopy cover (78.5%), half canopy cover (50%), sparse canopy covers (5%) for difference in temperature between surface and air dT , albedo α , roughness length Z_{om} , c (G/Rn), NDVI and selection of wet and dry pixel temperatures. The results concluded that the model is sensitive to selection of wet and hot pixel, dT and c (more than 35% for deviation in 50% of the base value) and least sensitive to NDVI, albedo and roughness length at full canopy cover. At half canopy cover, the model is

sensitive to selection of hot and wet pixel selection (more than 100% with 7.5K change in selection of cold pixel temperature), roughness length, c , dT and least sensitive to NDVI. At sparse canopy cover, the model is sensitive to selection of hot pixel (change in 270% in ET estimate with 12.5K change in selection of hot pixel temperature), NDVI and least sensitive to cold pixel selection and albedo.

This study focuses on sensitivity analysis on METRIC at two scales of error, Global error, Local error. *Global Error*: The systematic error is transferred to and potentially compensated by the calibration. *Local Error*: The error that is random and locally systematic and is not transferred into and compensated by the calibration. This research is conducted for different types of vegetative cover (corn, alfalfa, soybeans) for three different types of conditions (May 30, July 1 and September 27). Images from May 30, July 1, and September 27 represent, early growth, during growing, after growth conditions of the crops. The sensitivity of Crop coefficients (K_c or ET_rF) are tested in this study. Even small change produces considerable amount of errors in terms of percentage for K_c . So, the outputs are stated in terms of absolute values of ET_rF which is easy to understand the behavior of crops under various conditions.

Chapter 2: Materials and Methods

2.1 METRIC

The detailed description of Mapping Evapotranspiration with Internalized Calibration (METRIC) can be found at Allen et al. (2007a&b). The brief description of METRIC is described here. Evapotranspiration (ET) is calculated as residual energy of the surface energy balance equation

$$LE = R_n - G - H \quad (1)$$

Where LE is latent energy consumed by ET; R_n is Net radiation, G is Energy consumed by soil and H is sensible heat flux (Energy consumed in heating of air). All the units are in $W m^{-2}$.

Generally, the accuracy of LE depends on accuracy of calculation of R_n , G, H. But, METRIC eliminates all biases by internal calibration of sensible heat flux.

Net Radiation (R_n):

Net radiation is sum of the net short wave radiation and net long wave radiation given in the following equation

$$R_n = R_{s\downarrow} - \alpha R_{s\downarrow} + R_{L\downarrow} - R_{L\uparrow} - (1 - \epsilon_0) R_{L\downarrow} \quad (2)$$

Where $R_{s\downarrow}$ is incoming short wave radiation ($W m^{-2}$), α is surface albedo (Unit less), $R_{L\downarrow}$ is incoming long wave radiation ($W m^{-2}$), ϵ_0 is surface thermal emissivity (Unit less) and $R_{L\uparrow}$ is out going long wave radiation ($W m^{-2}$). The term $(1 - \epsilon_0) R_{L\downarrow}$ represents the fraction of reflected incoming long wave radiation.

The incoming short wave radiation is calculated as

$$R_{sl} = \frac{G_{sc} \cos \theta_{rel} \tau_{sw}}{d^2} \quad (3)$$

Where is G_{sc} is solar constant (1367 W m^{-2}), θ_{rel} is Sun incident angle, τ_{sw} is broad band atmospheric Transmissivity, d^2 is square of earth-sun relative distance.

τ_{sw} is calculated from the given equation from ASCE – EWRI (2005) as a function of atmospheric pressure, water in atmosphere, atmospheric mass and optical path length. $\cos \theta_{rel}$ is calculated equation given by Duffie and Beckman (1991) making use of latitude, hour angle, and declination of earth. d^2 is calculated as a function of day of year of the satellite image given by Duffie and Beckman (1991).

Albedo is calculated as integration of surface reflectivities with weighting functions of corresponding bands. For that we have to calculate the reflectance for each band using the digital numbers. Digital numbers are converted to radiance (L) using satellite constants and reflectance at top of atmosphere (ρ_t) is calculated as following equation.

$$\rho_{t,b} = \frac{\pi L_{t,b} d^2}{ESUN_b \cos \theta_{rel}} \quad (4)$$

Where $L_{t,b}$ is radiance at top of atmosphere for a band b $ESUN_b$ is mean solar exoatmospheric radiation at band b. $ESUN$ values are given by Chander and Markham (2003) for Landsat 4 and 5, LPSO (2004) for Landsat 7 and Tasumi et al. (2007) for MODIS.

Reflectance at surface ($\rho_{s,b}$) is calculated using ρ_t by following equation:

$$\rho_{s,b} = \frac{\rho_{t,b} - \rho_{a,b}}{\tau_{in,b} \cdot \tau_{out,b}} \quad (5)$$

Where $\tau_{in,b}$ and $\tau_{out,b}$ represents narrow band transmittances for incoming solar radiation and outgoing solar radiation. $\rho_{a,b}$ is path radiance.

$$\tau_{in,b} = C1 \exp \left[\frac{C2.Pair}{Kt.Cos\theta h} - \frac{C3.W + C4}{Cos\theta h} \right] + C5 \quad (5a)$$

$$\tau_{in,b} = C1 \exp \left[\frac{C2.Pair}{Kt.1} - \frac{C3.W + C4}{1} \right] + C5 \quad (5b)$$

Where, C1-C5 are constants and can be obtained from Allen et al. (2007a), Kt is clearness coefficient, θh is solar zenith angle, Pair is air pressure and W is precipitable water in the atmosphere.

Therefore, albedo is calculated as

$$\alpha = \int [\rho_{s,b} w_b] \quad (6)$$

w_b weighting functions can be found in Tasumi et al. (2008).

From (3) and (6) net shortwave radiation can be calculated.

Outgoing Long wave radiation is calculated by equation (7)

$$R_{L\uparrow} = \epsilon_0 \sigma T_s^4 \quad (7)$$

Where ϵ_0 is surface emissivity which is a function of leaf area index (LAI), σ is Stefan Boltzman constant ($5.67 \times 10^{-8} \text{ W m}^{-2} \text{ K}^{-4}$) and T_s is surface temperature calculated from equation (8)

$$T_s = \frac{K_2}{\ln[(\epsilon_{NB}K_1/R_c) + 1]} \quad (8)$$

Where K_2 , K_1 are satellite constants can be found in Allen et al. (2007a), ϵ_{NB} is narrow band emissivity calculated as a function of LAI and NDVI (Normalized difference vegetative Index) given by Tasumi(2003). R_c is thermal radiance calculated equation given by Wukelic et al. (1989).

Incoming long wave radiation is calculated using the equation provided below

$$R_{L\downarrow} = \epsilon_a \sigma T_a^4 \quad (9)$$

Where ϵ_a is atmospheric transmissivity given by Bastiaanssen (1995) and Allen et al. (2000) calculated as

$$\epsilon_a = 0.85(-\ln \tau_{sw})^{0.09} \quad (10)$$

T_a is near surface air temperature. In most of the METRIC applications surface temperature at the cold pixel is also used as near surface air temperature in Eq 10. From equations (7) and (9) net long wave radiation is calculated.

To sum up, from Equations (3), (6), (7), (9), net radiation (2) can be achieved.

Soil Heat flux (G):

Soil heat flux is energy used up by soil. It is calculated empirically as a ratio to net radiation given by Tasumi (2003) as a function of LAI, given by

$$\frac{G}{Rn} = 0.05 + 0.18 e^{-0.521 LAI} \quad (\text{For } LAI \geq 0.5) \quad (11a)$$

$$\frac{G}{Rn} = 1.80(T_s - 273.15) / R_n + 0.084 \quad (\text{For LAI} < 0.5) \quad (11b)$$

Sensible Heat flux (H):

Sensible heat flux is energy used in heating of the air and is calculated using the following equation

$$H = \rho_{\text{air}} C_p dT / r_{\text{ah}} \quad (12)$$

Where ρ_{air} is density of air , C_p is specific heat of air at constant pressure, r_{ah} is aerodynamic resistance between heights z_1 and z_2 , and dT is difference in temperature between heights z_1 and z_2 . C_p is constant ($1004 \text{ J Kg}^{-1} \text{ K}^{-1}$). To compute r_{ah} , Monin-Obukhov theory is applied in an iterative process considering buoyancy effects until r_{ah} is stabilized.

dT is assumed to have a linear relationship with surface temperature T_s and is written as

$$dT = b + aT_s \quad (13)$$

To get coefficients a, b and r_{ah} , hot and cold pixels have to be selected from the image. Hot pixel should have to be from high temperature, bare agricultural soil and cold pixel should have to be from well irrigated highly vegetated surface with low temperature. Then sensible heat flux at cold H_{cold} and hot pixel H_{hot} are calculated as follows:

$$H_{\text{cold}} = Rn - G - 1.05 \lambda ET_r \quad (14)$$

$$H_{\text{hot}} = Rn - G - K_c \lambda ET_r \quad (15)$$

Where ETr is 0.5 m tall alfalfa based reference evapotranspiration calculated using ASCE standardized Penman-Monteith equation (ASCE –EWRI 2004) using quality weather data from local weather station. Kc is calculated using soil water balance model, usually varies from 0.05 to 0.15. Now dT_{cold} , dT_{hot} are calculated using inverse of equation (12). Equations (16) (17) and (18) give values for aerodynamic resistance, friction velocity, momentum roughness length.

$$r_{ah} = \frac{\ln\left(\frac{z_2}{z_1}\right) - \psi_{h(z_2)} + \psi_{h(z_1)}}{u_* \times k} \quad (16)$$

$$u_* = \frac{ku_{200}}{\ln\left(\frac{z_2}{z_1}\right) - \psi_{m(200)}} \quad (17)$$

Where z_2 , z_1 heights above zero plane displacement of the vegetation, k is von kormans constant (0.41), u_* is friction velocity, ψ_{hz1} and ψ_{hz2} are stability correction factors for heat transport at heights z_1 , z_2 , $\psi_{m(200)}$ is stability correction factors for momentum transport at height 200m, z_{om} is momentum roughness length, u_x is wind speed recorded from weather station at height z_x . Generally, $z_1 = 0.1$ m and $z_2 = 2.0$ m.

$$z_{om} = 0.12 h \quad (18)$$

Where, h is canopy height near the weather station. Eq 18 is used for calculation of momentum roughness length near weather station.

Z_{om} is calculated using land use map for rest of the image. dT_{cold} , dT_{hot} are calculated in secondary model and embedded them into primary METRIC model. Using dT_{cold} , dT_{hot} initial values of coefficients a, b are obtained through which H is calculated for each pixel using (12) and (13). Later Monin Obukhov length L is calculated to examine the stability conditions and through which stability factors for momentum and heat transport is calculated (Allen et al. 2007a). Later, friction velocity and aerodynamic resistance are calculated as a function of stability correction factors. These values are then used to calibrate the model again. This process is continued until aerodynamic resistance and dT_{hot} are stabilized. The final values of coefficients a, b are the calibration constants to the model. And sensible heat flux H is calculated using (12) for each pixel.

Latent heat flux (LE) or Instantaneous ET:

Latent heat of vaporization is calculated for each pixel using equation (1).

Instantaneous ET at satellite over pass time

$$ET_{inst} = 3600 LE / \lambda \quad (19)$$

Where λ is latent heat of vaporization and is given by

$$\lambda = (2.501 - 0.00236(T_s - 273)) \times 10^6 \text{ J Kg}^{-1} \quad (20)$$

Reference ET fraction or crop coefficient ET_rF is calculated as

$$ET_rF = ET_{ins} / ET_r \quad (21)$$

The 24 hour ET is calculated using the following equation

$$ET_{24} = ET_rF \times ET_{r-24} \quad (22)$$

Where ET_{r-24} is cumulative 24 hour ET_r for the day of the image. The seasonal of periodical ET can be obtained by interpolating ET_rF from one image date to another and by cumulative 24 hour ET_r for that period.

The whole model is written and executed in MATLAB environment except the selection of hot and cold pixel sensitivity is done manually, using conventional ERDAS imagine and spreadsheets.

2.2 Weather station and site conditions

This study is conducted in South central Nebraska, using Landsat path 29, Row 32 image. Coordinates for center of the image are roughly 40.33 °N, 98.04 °W. The automated weather data network (AWDN) station at Clay center (40.57° N, 98.13° W) operated by the High Plains Regional climatic center (HPRCC) data is used as input to the METRIC model used in this study. The distance between center of the image and weather station is roughly 27 km. All the selected croplands are center pivot irrigated and soils are silt loam (Soil survey staff, accessed: 2011).

2009 Landsat TM images from May 30, July 1 and Landsat ETM+ image from September 27 is used in this study. All the images are free of clouds and any other disturbances. Study area of 1300 X 1300 pixels is chosen near centre of the image which has wide variety of land covers, to reduce the run time of each model.

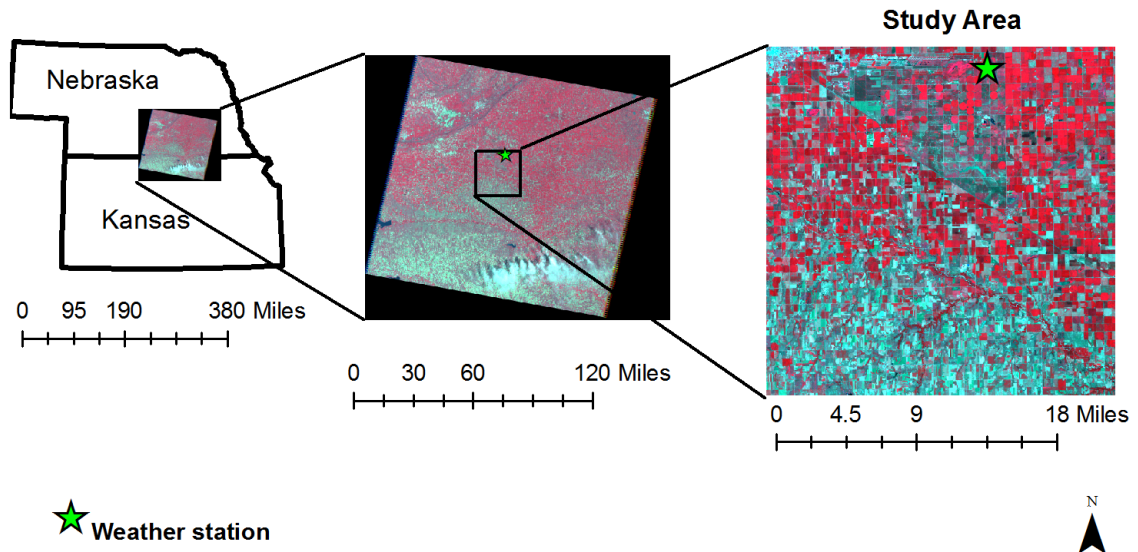


Figure 1: Weather station location and study area

Fourteen fields for each crop type are selected using the National Agricultural Statistics Service (NASS) 2009 land cover map. The user's accuracy of corn, soybeans, alfalfa reported by NASS is 98.64%, 97.44% and 89.09%. These selected fields are used for analysis from image to image.

The site conditions for three different images are given in table 1. The May image is almost full of bare soils on agricultural fields, which is evident from range and average NDVI values in May. But few alfalfa fields have vegetation where its maximum NDVI went all the way to 0.821, but its average NDVI is 0.521. So, the selected fields for alfalfa have wide variety of conditions from full grown vegetation to residual stubble and young leaves. Corn and soybeans does not have big variations in surface conditions, which can be observed through surface temperatures.

On July image, the range for NDVI and T_s for corn and alfalfa is minimal, whereas, soybeans show variations in T_s , NDVI from minimum 308 K, 0.318 to

maximum 315.7 K and 0.647. So, in July, all corn, alfalfa surface conditions are similar, but soybeans surface conditions vary from mixed conditions to hot pixel conditions, because only 2 fields out of 14 selected fields have NDVI above 0.6. Soybeans might have late planted, so, there is little vegetation on July 1st. However, they have reached their peak growth in August, which is observed from acquired Landsat 5 image dated August 2nd 2009 (Not shown here).

On September image, the surface conditions for alfalfa are fully vegetated. Even though the minimum NDVI value reports 0.505, that is the only field that has NDVI less than 0.7. Again the average NDVI for alfalfa is greater than 0.7. Corn and soybeans have similar NDVI ranges, but surface temperature is slightly high for soybeans. So, soybeans have bare soil conditions for all fields except one field reporting an NDVI of 0.55 which is a vegetative pixel. This is because of the late plantation of soybeans in 2009, which is evident from the fully vegetated soybean pixels in October 2009 landsat image (not shown in this study). Corn fields have bare soil conditions but, with smaller temperatures than soybean fields.

		May			July			September		
		Corn	Soybeans	Alfalfa	Corn	Soybeans	Alfalfa	Corn	Soybeans	Alfalfa
NDVI	Min	0.216	0.156	0.237	0.753	0.318	0.657	0.203	0.215	0.505
	Max	0.310	0.266	0.824	0.816	0.647	0.837	0.414	0.555	0.793
	Avg	0.259	0.198	0.521	0.791	0.459	0.784	0.315	0.310	0.736
T _s (°K)	Min	304.9	306.4	300.1	298.5	308.4	299.0	292.4	294.6	290.9
	Max	317.4	317.4	315.2	301.5	315.7	302.2	294.2	297.2	293.0
	Avg	314.5	313.6	309.3	299.8	312.2	300.6	293.0	296.0	291.7
Albedo	Min	0.129	0.146	0.158	0.144	0.180	0.158	0.098	0.113	0.129
	Max	0.229	0.237	0.212	0.195	0.207	0.223	0.180	0.177	0.204
	Avg	0.188	0.204	0.179	0.170	0.191	0.192	0.122	0.134	0.179
ET _F	Min	0.260	0.280	0.277	0.921	0.384	0.839	0.412	0.383	0.417
	Max	0.845	0.774	1.028	1.028	0.673	0.951	0.739	0.731	0.771
	Avg	0.394	0.426	0.638	0.972	0.516	0.903	0.582	0.576	0.650
G (Wm ⁻²)	Min	113.6	114.1	38.9	40.4	61.2	35.4	77.5	76.1	33.6
	Max	126.1	125.22	123.1	54.1	119.7	69.5	84.2	93.4	90.1
	Avg	121.1	118.9	89.5	46.6	94.7	44.6	81.0	84.6	43.4
ETr(mm/h)	1.0019			0.627			0.798			
U(m/s)	4.63			1.815			7.65			

Table 1: Site conditions and Base values of different parameters, for three different images. Min, Max, Avg represent Minimum, Maximum, Average of fourteen selected fields for each crop type.

Chapter 3: Global Error

3.1 Methodology

For the global scale sensitivity analysis, two different cases are considered. *Input bias*: The errors from input data and *Calibration Bias*: The errors incurred in process of calibration. The variables considered for input bias are: Reflectance at satellite (ρ_t), Transmissivity (τ), Wind speed (u), Incoming Long wave radiation (R_{li}) and Reference Evapotranspiration (E_{Tr}).

For calibration bias, selections of different hot and cold pixels are considered. For input bias, variables are changed -50%, -25%, -10%, 0, 10%, 25%, 50% for u, E_{Tr} from their base values and τ is deviated -25%, -15%, -5%, 0, 5%, 15%, 25% from their base values because $\pm 25\%$ is too unrealistic. The reflectance values are doubled and halved, because the values are small and their deviations will be too small if varied from -50% to +50%. For the calibration bias, colder pixels are selected at -3, -2, -1, -0.5 °K (approximately, as it is difficult to find the pixels with exact differences) than the original hot pixel and warmer pixels at +3, +2, +1, +0.5 °K are selected than the original cold pixel.

For input bias, the whole METRIC model is programmed in MATLAB, and cold pixel selection is automated such that the pixel has maximum NDVI, and minimum T_s match. The hot pixel is also automated in the same way, such that the pixel has minimum NDVI and maximum T_s match. In this chapter, the parameter considered, is deviated

from the baseline value and the model is run such that the calibration is done for each changed value. In other words, the error is passed through the calibration.

3.2 Results and Discussion

All the curves presented in the following sections are average curves of all 14 fields for each crop type. The error bars in the figures describe the maximum and minimum values of ET_rF for each crop type.

3.2.1 Reflectance at satellite (ρ)

Errors in reflectance can cause due to various reasons like transmittance (Stowe et al.1997), calibration artifacts (Vogelman et al. 2001), canopy structure shading (Li et al.1992; Leblon et al. 1996; Ekstrand 1996) shadows of nearby objects (Teillet et al.2001), topography (Levin et al. 2004; Schaepman-strub et al. 2006). Transmittance error is dealt separately in the next section.

Vogelman et al. (2001) reported maximum of 8.4% change in upwelling radiance for band2 of Landsat 5 and maximum of 6.0% change in upwelling radiance for band2 of Landsat 7 when MODTRAN models are compared with the field measurements. Leblon et al. (1996) found that there is more than 50% error in mean reflectance in near infrared region (NIR) for grass land and in visible region for bare soil due to various kinds of shadows. Moran et al. (1995), got error up to 0.05 in visible region for dark target and up to 0.1 in NIR for bright target. Calibration artifacts are due to radiometric errors or geometric errors. Geometric errors caused by interfocal plane offsets can cause errors in pixel offsetting (Vogelmann et al. 2001) there by affecting the reflectance.

Helder et al. (1997) reported that the error due to memory effect (ME) of the sensor could be in the order of multiple digital numbers (DN). And Helder et al. (1996) reported change in DNs could be less than 1 DN due to scan correlated shift. Coherent noise may cause an error upto 0.25 DN (Helder 1999).

Table 2 shows errors in reflectance caused by deviation of 1 DN for a randomly selected vegetative and bare soil pixel on the May 30 2009 image.

	Change in radiance for 1 DN change (W/m ² /sr/ μ m)	Change in Reflectance	Reflectance at selected vegetative pixel	Reflectance at selected bare soil pixel	% change in reflectance at selected vegetative pixel	% change in reflectance at selected bare soil pixel
TM1	0.76	0.0014	0.095	0.147	1.48	0.95
TM2	1.44	0.0028	0.081	0.159	3.52	1.79
TM3	1.04	0.0024	0.053	0.183	4.56	1.32
TM4	0.87	0.003	0.504	0.28	0.60	1.08
TM5	0.12	0.002	0.197	0.399	1.02	0.50
TM7	0.07	0.0029	0.079	0.338	3.70	0.86

Table 2: Absolute and percentage change in radiance and reflectance for 1 DN change in randomly selected cold and hot pixels for Landsat 5.

We can see if 1DN is changed, 4.56 % reflectance is changed for band 3, 3.5% change in band2 for cold pixel and 3.7% change in band7 for cold pixels. The hot pixel

reflectances are least sensitive to DN change compared to that of a cold pixel. So, error caused by ME in reflectance of band 3 alone can exceed 10%.

Even though different bands have different sensitivities, this paper tests the reflectance errors at -50% and +200% (halving and doubling) of the original reflectance of all the bands to get better understanding of the effect on final ET product.

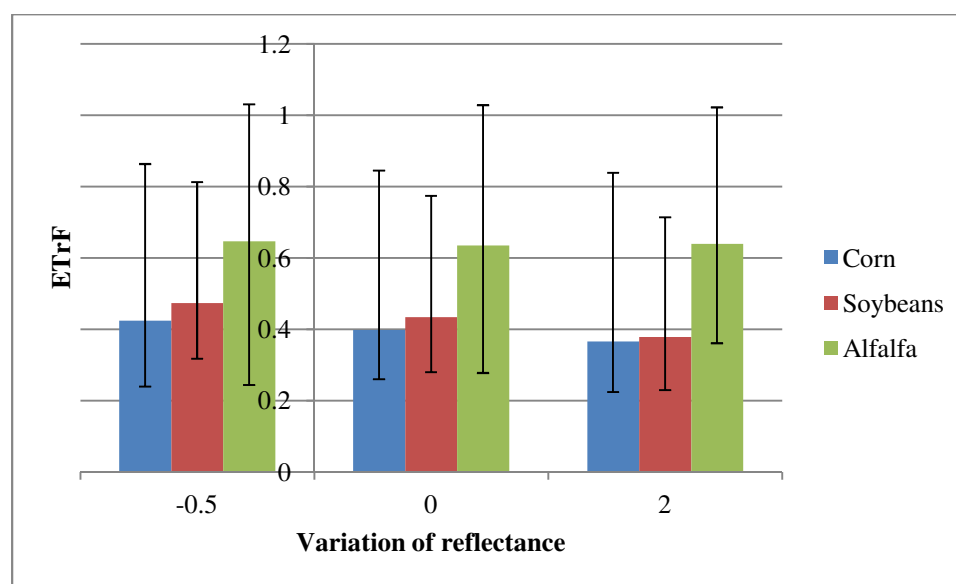


Figure 2: Sensitivity to reflectance on May 30 2009

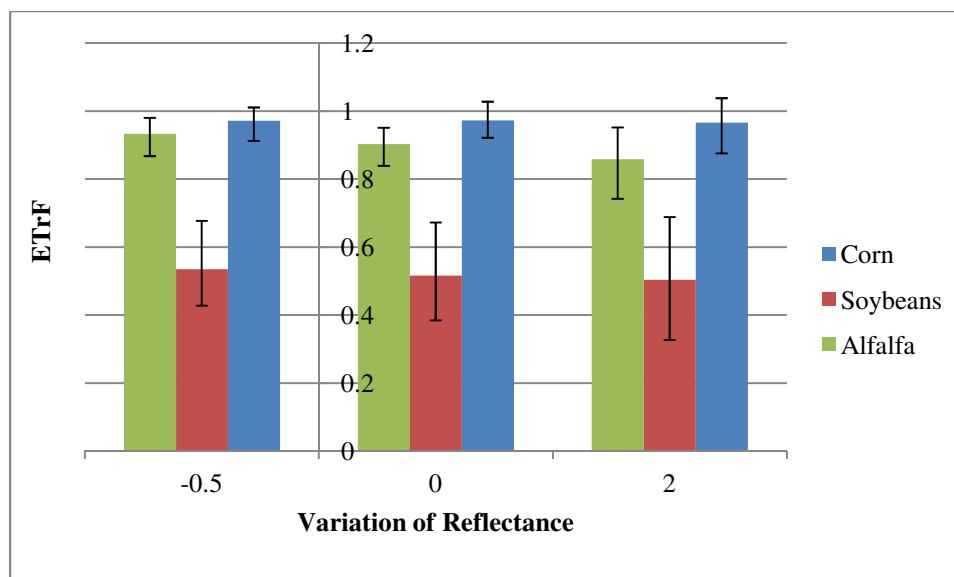


Figure 3: Sensitivity to reflectance on July 1 2009

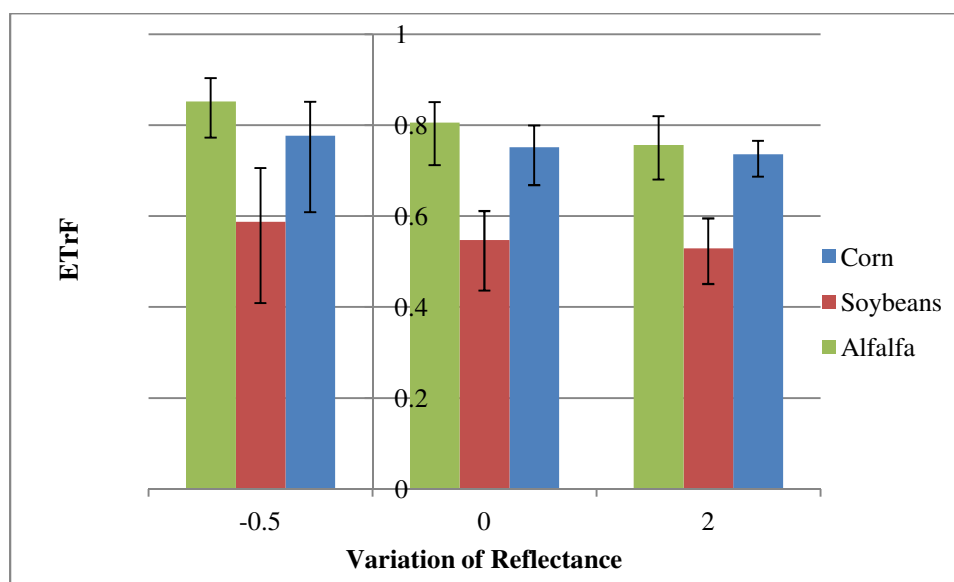


Figure 4: Sensitivity to reflectance on September 27 2009

The hypothesis is, when reflectance decreases, albedo decreases, outgoing short wave radiation decreases so that the available energy for ET increases, and ET should increase. ET decreases, with increase in reflectance. Figures 2-4 show the variations of ET_rF to the bias in reflectance at top of the atmosphere for May, July, September images

respectively. For all the images, the final ET_rF values agree with our hypothesis, but 100% increment and 50% decrement did not change the average ET_rF values more than 11% combined of all images, which shows the METRIC's capability of internalized calibration to adjust H, to get ET values in agreement with the weather station's ET. 11% of error is caused due to rounding of digits. The range variations are due to the persistent residual error after calibration. However, the input error introduced is +100% and -50%, but the deviations in final ET_rF values are around 10%. So, the internal calibration potential is evident from the above results.

	$\partial ET_rF / \partial \rho$		
Image month	Corn	Soybeans	Alfalfa
May	0.07/150%	0.12/ 150%	0.01/150%
July	0.01/150%	0.03/150%	0.07/150%
September	0.04/150%	0.06/150%	0.1/150%

Table 3: Absolute change in average ETrF when reflectance is changed, for all images considered.

Table 3 shows the absolute change in average ETrF when reflectance is changed from -50% to +100%, for various months and different crop types.

3.2.2 Transmittance error (τ)

In METRIC, the equation used for Transmissivity is similar to the equation proposed by Allen et al. (1998) but by eliminating turbidity co-efficient, making the calculations simple. And the Transmissivity calculation is limited to low haze conditions. The purpose of testing sensitivity of Transmissivity is to know the behavior of the model during hazy atmospheric conditions. The haze can be caused due to smoke emitted by the

vicinity of local forest fires, fire accidents, volcanic eruptions and haze created by fertilizers, imperceptible clouds. Also due to air pollution, aerosols may have affect on atmospheric turbidity (Chameides et al. 1999; Mani et al. 1973). Mani et.al. (1973) noticed doubling of turbidity values in ten years over tropics.

Also, the ozone layer thickness may get fluctuations in transmittance estimate. Ozone layer thickness varies with latitude (Yang et al. 2006). Ozone absorbs infrared radiation (Wulf, 1930). Therefore, we can conclude, the places with ozone depleted layer may have increased NIR radiation but no significant affect in visible region.

To make our analysis simple, assumption is made that the transmittance from all the bands are equally affected. But in reality, different bands react differently for same change in haze or aerosol concentration (Tasumi et al. 2008).

So, the model is checked for transmittance errors, beyond their workable limits even though it is unrealistic: just to check the model capability of blunders in input data. The biases are introduced in both narrowband and broadband transmittances.

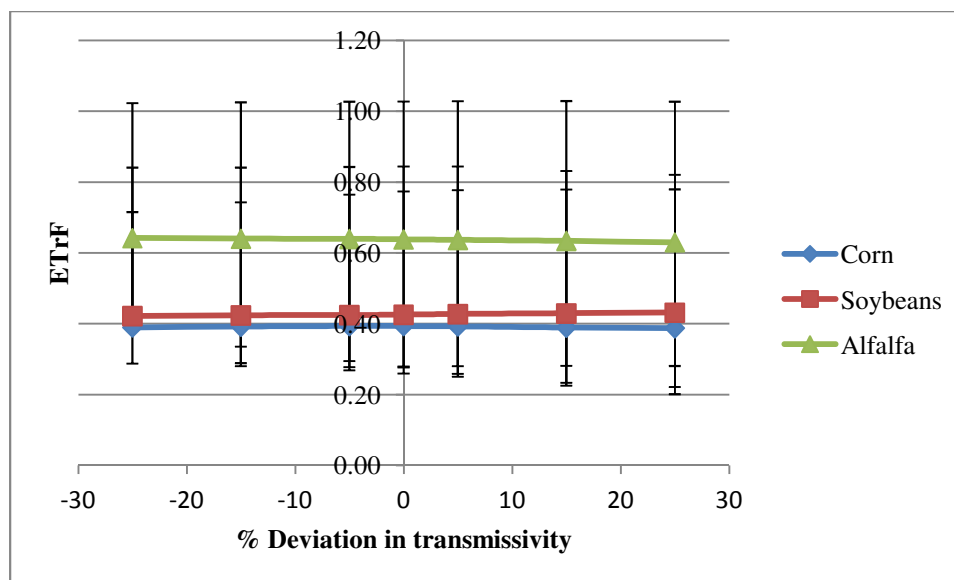


Figure 5: Sensitivity to Transmittance on May 30 2009

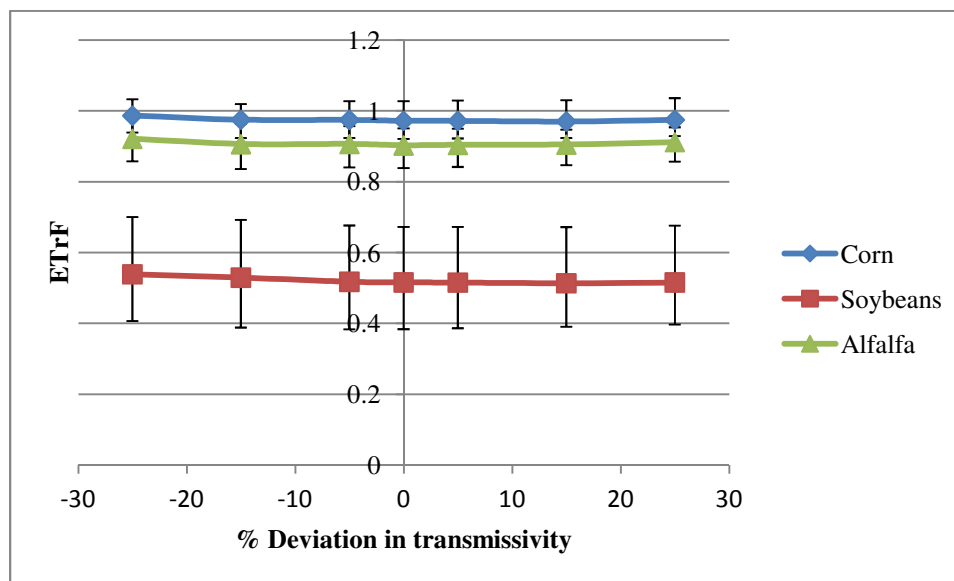


Figure 6: Sensitivity to Transmittance on July 1 2009

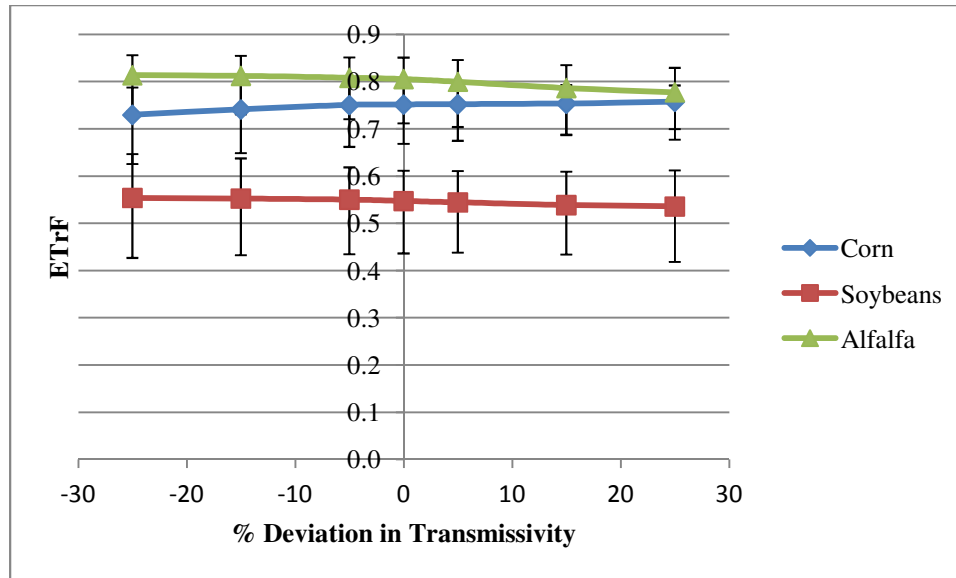


Figure 7: Sensitivity to Transmittance on September 27 2009

Our hypothesis is, when the atmospheric, turbidity decreases and clearness of sky increases, transmissivity is decreased. Due to this change, the incoming solar radiation increases, and incoming long wave radiation is decreased, because incoming long wave radiation is dependent on cloud cover and aerosols and water vapor (SICART et al.1999). The affect of net long wave radiation is smaller than incoming solar radiation (R_{si}) on net radiation during day time because R_{si} is dominant. Ideally, when transmissivity increases, more energy passes through the atmosphere reflecting more energy to satellite, leading to increase in reflectance. But, this change in transmissivity is an error introduced manually. So, reflectance at satellite ρ_{sat} remains unchanged because, in METRIC, calculation of reflectance at satellite is independent of transmissivity of the atmosphere, but dependent on radiance values. But at-surface reflectance is inversely dependent on narrow band transmittances. Numerically, surface reflectance is decreased, when transmissivity is increased. Because of this, albedo decreases and outgoing short wave radiation is

decreased and also, incoming short wave radiation is increased, so that energy available for ET is increased. The same is true vice versa.

Figures 5-7 show the sensitivity of model to transmissivity for May, July, September images. For all the images, for all crop types, the ET_rF curves are flat, representing the METRIC's capability of compensating the systematic errors through internal calibration. Appendix A shows the variations of a, b to vary H to provide consistent ET_rF values for May image. The slight variations in the curves are due to rounding off the digits. Even though the range is slightly varying in May image for minimum ET_rF values, the deviation is minimal.

	$\partial ET_rF / \partial \tau$		
Image month	Corn	Soybeans	Alfalfa
May	~0/50%	-0.01/ 50%	0.01/50%
July	0.01/50%	0.02/50%	0.01/50%
September	-0.03/50%	0.02/50%	0.04/50%

Table 4: Absolute change in average ET_rF when transmissivity is changed, for all images considered.

Table 4 shows the absolute change in average ET_rF when transmissivity is changed from -25% to +25%, for various months and different crop types.

3.2.3 Surface Temperature (T_s)

The errors can be due to the coarse resolution of thermal band in Landsat 5 and 7 compared to that of remaining bands. Resampling of the thermal band may not represent the exact thermal radiance of a land cover, especially in heterogeneous land surface types.

The systematic errors in estimation of surface temperature can be due to the combination of surface, atmospheric and instrumental effects (Jacob et al. 2004). Results obtained by Nerry et al. (1998), Petitcolin and Vermote (2002) confirmed the accuracy of 1 K in estimating radiometric temperature through Temperature- Independent Spectral Indices of Emissivity (TISIE) algorithm using MODIS data. Jacob et al. (2002) compared the ASTER and MODIS sensors for estimating brightness temperature and found that the difference is close to 0.5 °K and emphasized the necessity of using different atmospheric profiles when the spatial variability of study area is large.

Our hypothesis is, change in surface temperature will have direct effect on net long wave radiation component and sensible heat flux component. Increase in surface temperature decreases the net long wave radiation as the outgoing long wave radiation is dominant during day times and increases sensible heat flux H through dT as dT is linearly related to surface temperature. Since, sensible heat flux is more significant than the net long wave radiation especially at warm pixels, the net energy available to ET decreases. On the other hand, if surface temperature decreases, ET increases.

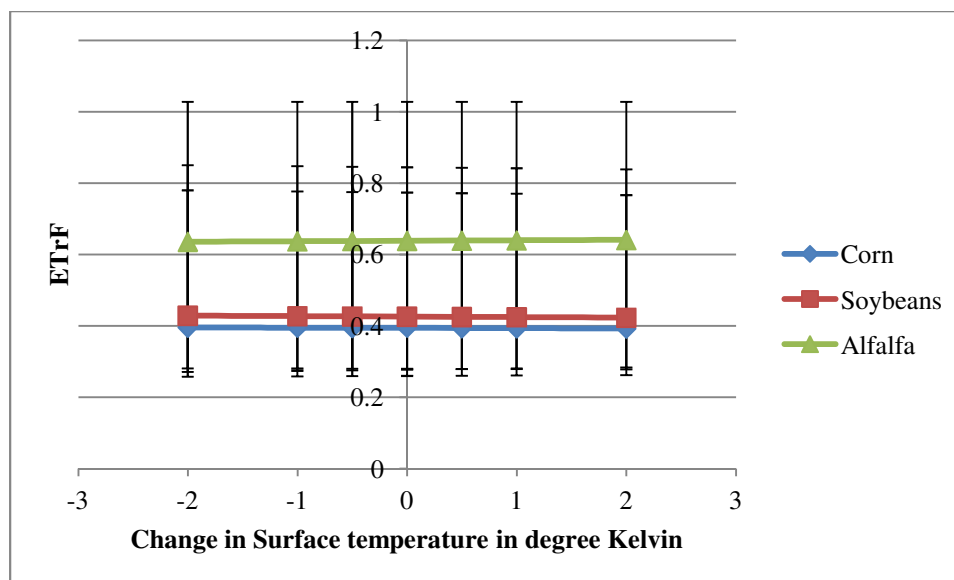


Figure 8: Sensitivity of model to T_s at global scale, on May 30 2009

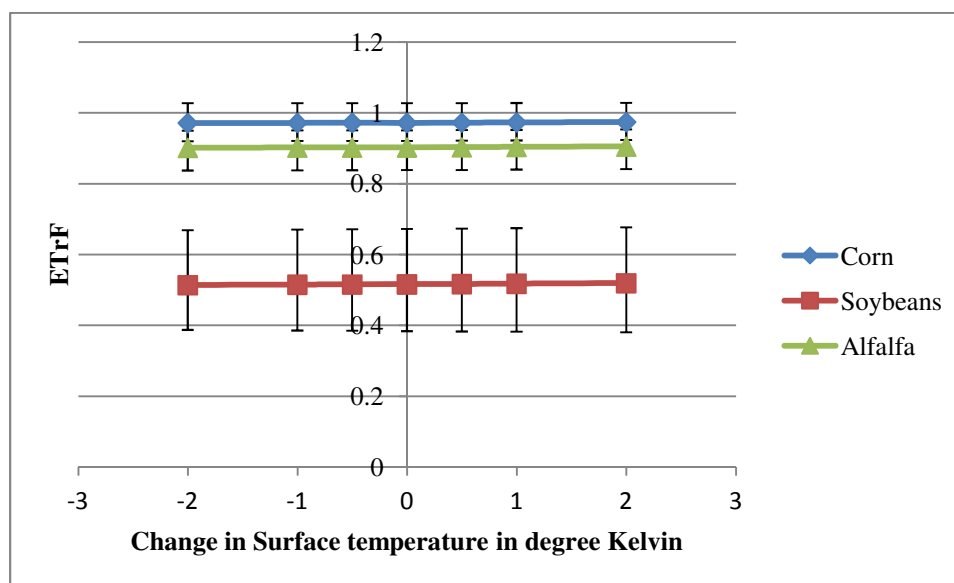


Figure 9: Sensitivity of model to T_s at global scale, on July 1 2009

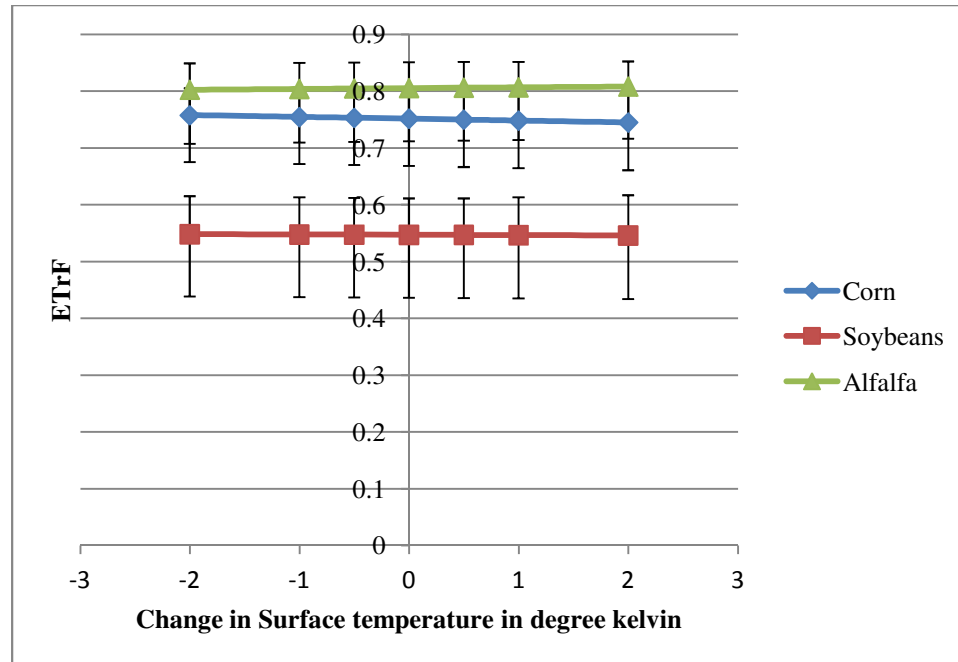


Figure 10: Sensitivity of model to T_s at global scale, on September 27 2009

Figures 8-10 show the variations in ET_{rF} with change in surface temperature for May, July, September images. For all the seasons, irrespective of the crop type, ET_{rF} curves are flat contradicting our hypothesis. This is because of the adjustments in calibration coefficients to match the ET_r at the cold pixel and assignment of fixed ET_{rF} at the hot pixel. Appendix A show the variations in calibration coefficients a , b with change in ET_r for May image. The curves are complementary to each other, to adjust the sensible heat flux in order to match the ET values obtained from the model with ET_r . This shows the METRIC's ability to calibrate internally to give consistent results in accordance with the weather station cancelling out the minor systematic errors.

Table 5 shows the absolute change in average ET_{rF} when surface temperature is changed globally from -2°K to $+2^{\circ}\text{K}$ for various months and different crop types.

	$\partial ET_r F / \partial Ts$		
Image month	Corn	Soybeans	Alfalfa
May	~0/°K	~0/°K	~0/°K
July	~0/°K	~0/°K	~0/°K
September	~0/°K	~0/°K	~0/°K

Table 5: Absolute change in average ETrF when surface temperature is changed, for all images considered.

3.2.4 Reference Evapotranspiration and wind speed (ET_r & u)

These are the key input data from a weather station required for calibration of the model. One should check the quality of these data to be good enough to obtain accurate spatial ET trends (Gowda et al. 2008). Instead of considering all parameters from weather station individually, sensitivity of ET_r is checked to compensate rest of the variables, as they contribute to the calculation of ET_r . Wind speed is considered separately because it affects the sensible heat flux. Errors can be from poor quality of weather data, poor instrumentation (Allen et al. 2005) and from user misinterpretation and miscalculations. To maintain consistency in the analysis, all the parameters are pushed up to $\pm 50\%$ of their original value to check the sensitivity of the model.

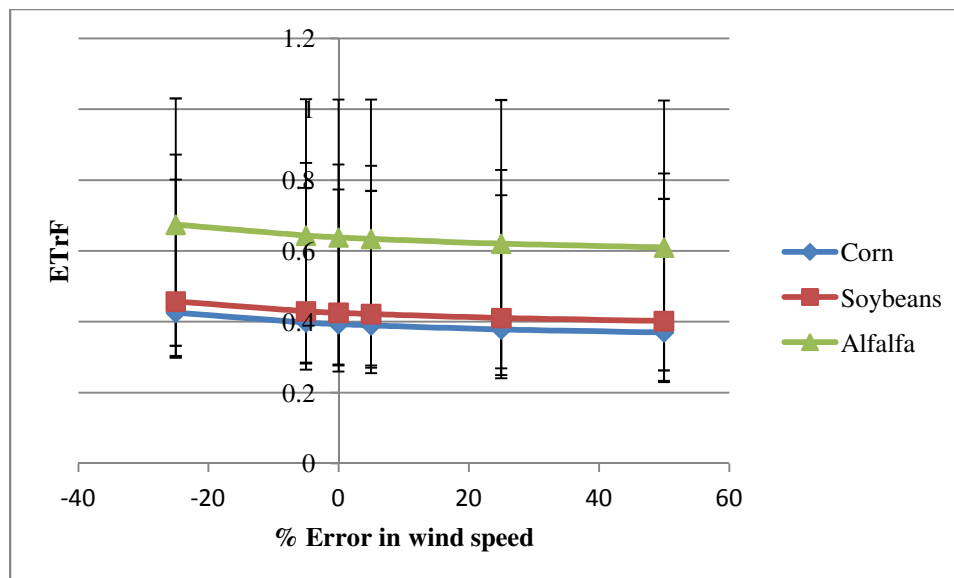


Figure 11: Impact of wind speed variations on the model for May 30 2009

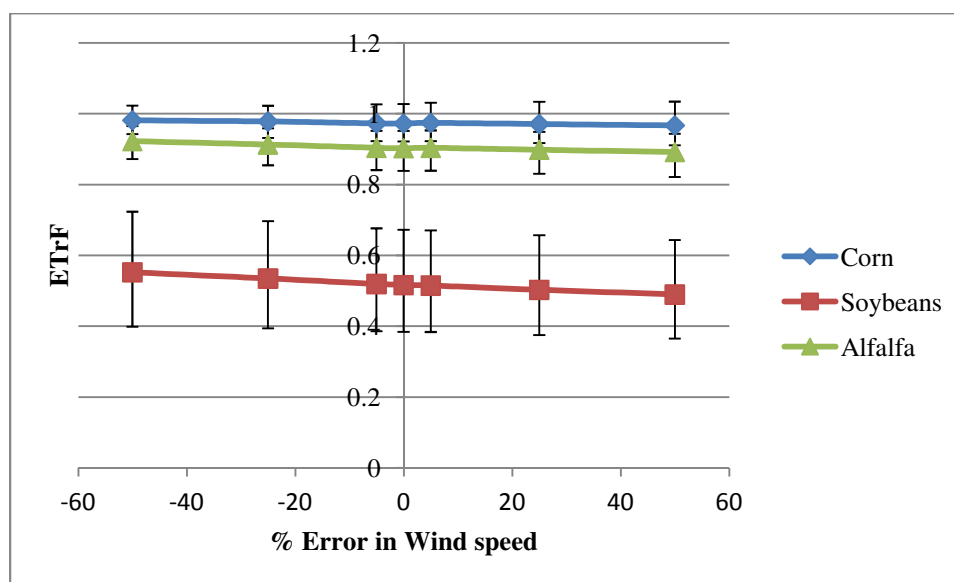


Figure 12: Impact of wind speed variations on the model for July 1 2009

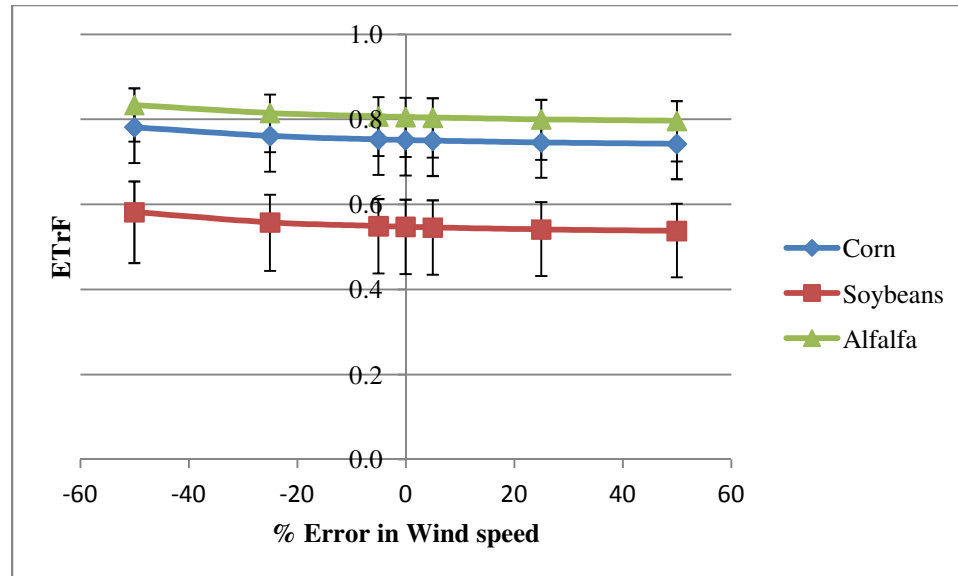


Figure 13: Impact of wind speed variations on the model for September 27 2009 image

The hypothesis is, when wind speed increases, the mixing of air increases, thereby decreasing the resistance to heat transfer. Consequently, sensible heat increases and the energy for ET decreases. Applying the same argument, ET increases, with decrease in wind speed. Figures 11-13 depict the variations in ET_rF for errors in wind speed for May, July, September images.

For all of the images, the results are as hypothesized, irrespective of the crop type, except for September image. For September (Figure 16), the model resulted in consistent ET_rF values, at higher wind speeds. The consistency is observed up to 75% of the original wind speed and deviation is witnessed from that point. Also, for May image, the ET_rF values at 50% u are unavailable because of the numerical instability obtained because of lower wind speeds. Allen et al. (2009) found that the numerical instability arises when wind speed at 200m is too low and suggested a minimum wind speed at 200m to be 4 m/s.

	$\partial ET_r F / \partial u$		
Image month	Corn	Soybeans	Alfalfa
May	0.06/75%	0.05/75%	0.06/75%
July	0.01/100%	0.06/100%	0.03/100%
September	0.04/100%	0.04/100%	0.04/100%

Table 6: Absolute change in average ETrF when wind speed is changed, for all images considered.

Table 6 shows the absolute change in average ETrF when wind speed is changed from -50% to +50% for various months and different crop types.

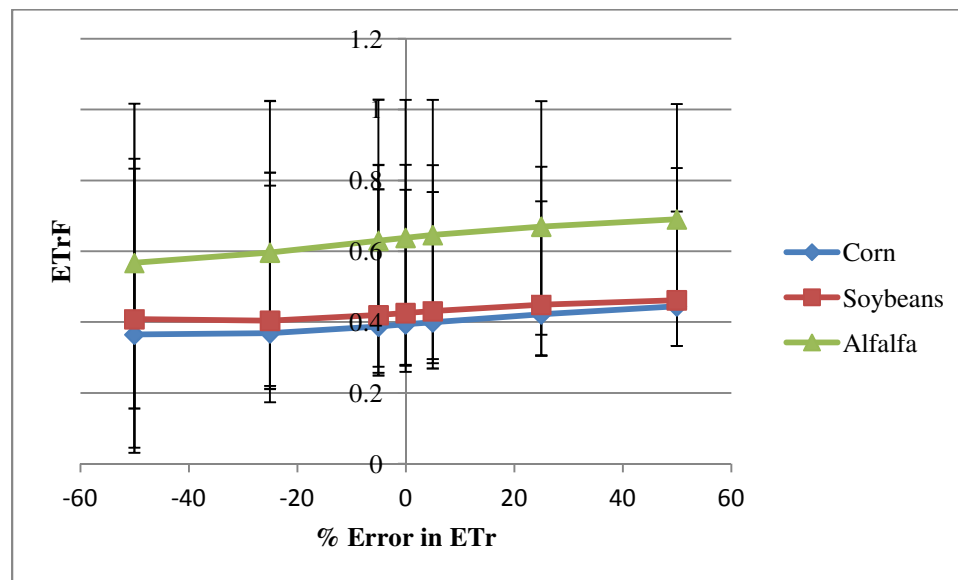


Figure 14: Model sensitivity to Reference evapotranspiration on May 30 2009

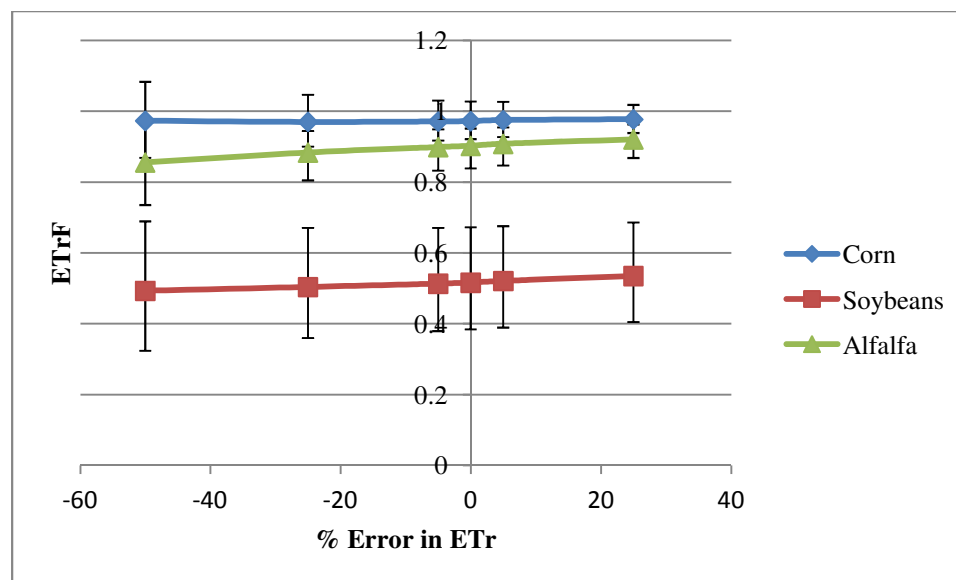


Figure 15: Model sensitivity to Reference evapotranspiration on July 1 2009

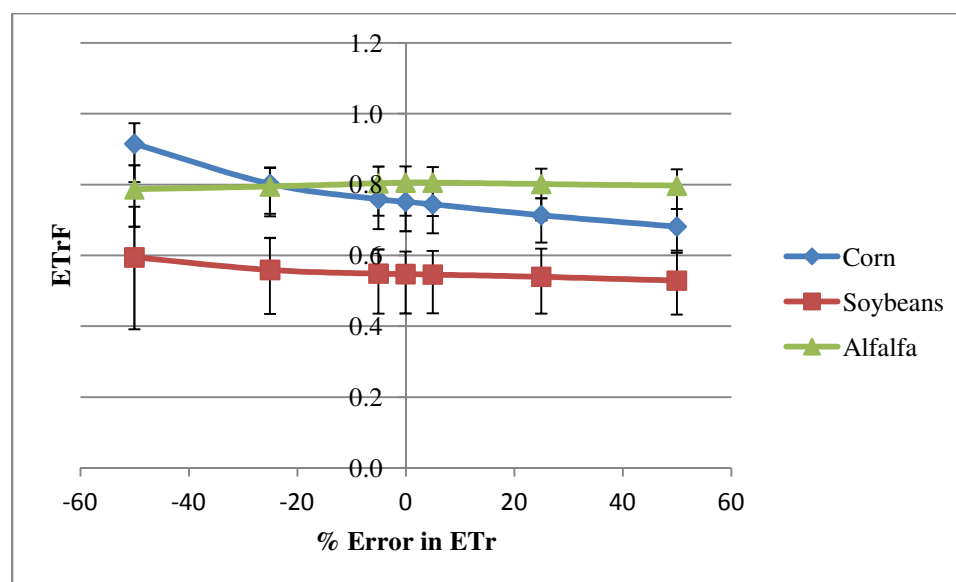


Figure 16: Model sensitivity to Reference evapotranspiration on September 27 2009

Instantaneous ET, suppose to decrease, when ET_r decreases. This is because of the calibration of model using ET_r obtained using Penman–Monteith equation and local weather station data. Figures 14-16 show the variation of ET_rF with change in reference

evapotranspiration (ET_r) for May, July, September images. The characteristics of curves are different for different images.

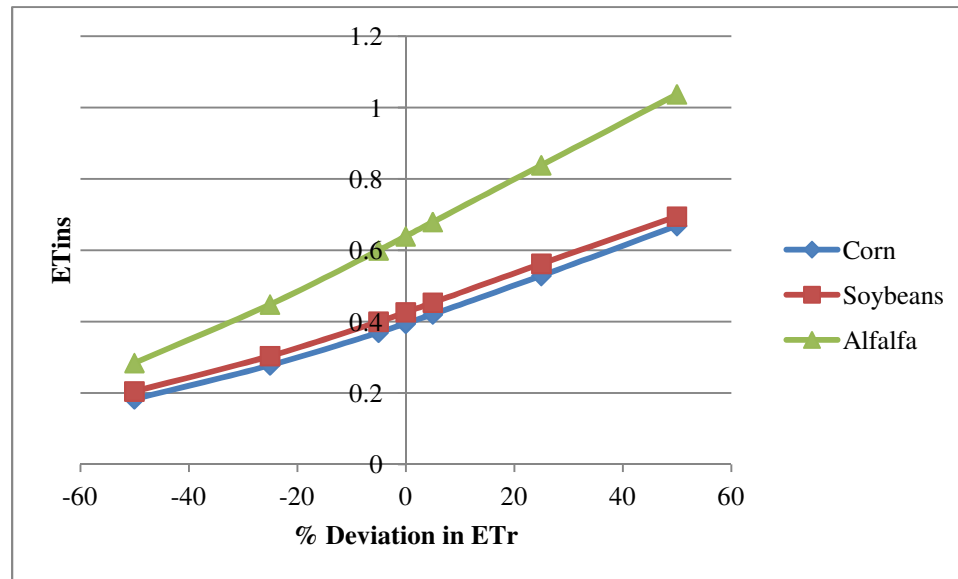


Figure 17: Instantaneous ET variations for May 30 2009 image

For the may image (figure 14), Alfalfa curve is different from corn and soybeans. Since, crop coefficient K_c at cold pixel is higher than K_c at hot pixel; the response to the variations of ET_r is significant at cold pixels and less significant at hot pixels. Because, at hot pixel, H is independent of ET_r , in ideal conditions. So, any change in ET_r , affects the $ET_r F$ at hot pixel lower than at the cold pixel. So, the sensitivity to change in ET_r at cold pixels is almost proportional. So, for all the images, the crop fields having the vegetation have their curves almost flat. In May image (Figure 14), even though many of alfalfa fields have vegetation, the curve is not flat because of the presence of dry fields in the selected 14 fields. Corn and Soybeans bare soil conditions for almost all of the fields. So, the curves are parallel, but not flat. The curve slope depends on the field conditions. The field conditions, close to the cold pixel's field conditions have flat curves and sloped

curves for pixels having different cold pixel temperature. However, the instantaneous ET is proportional to the ET_r , for any season, for any land surface type, which is evident from figures 17-19. Figure 17 shows the response of average ET_{ins} of 14 fields for each crop type with variations in ET_r . Again, the slope of ET_{ins} curve depends on surface temperature.

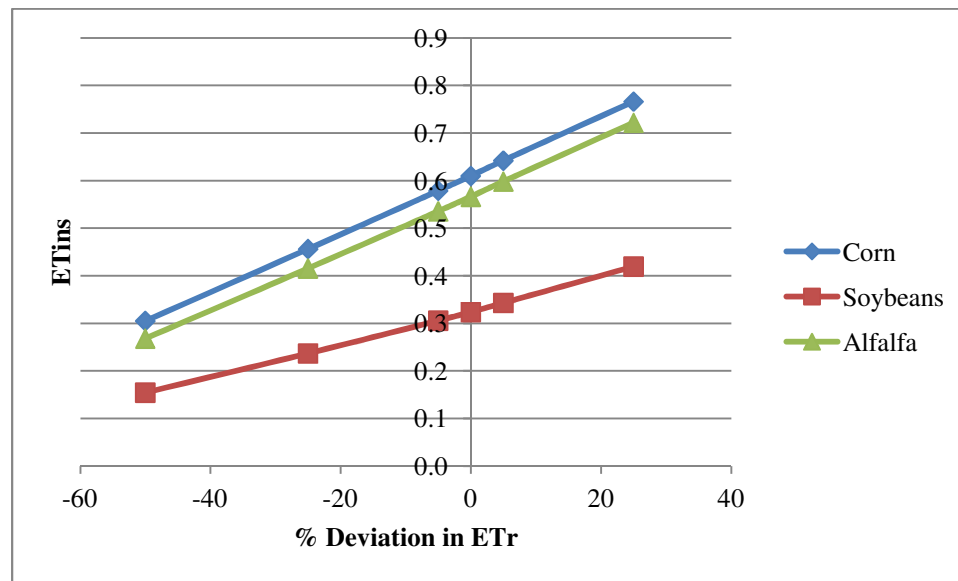


Figure 18: Instantaneous ET variations for July 1 2009 image

For July image (figure 15), the curves are almost horizontal for corn fields which have full vegetation for almost all of the 14 fields selected. The different slopes between corn and alfalfa is due to the surface temperature (See table 1) differences between corn and alfalfa, even though the NDVI for both crops is similar. Due to low surface temperatures, H is negative and moreover, Z_{om} impacts, the low H values in case of corn. The soybean curve is different from corn, because of the bare soil conditions having high surface temperatures and low NDVI values. Figure 18 shows average ET_{ins} variations for July image. We can see the nice straight lines of corn and soybeans parallel to each other,

but different slope for the soybean curve. Since the change in ET_{ins} is proportional to change in ET_r , we see almost flat ET_rF curves (Figure 15) for all crop types.

At +50% of the ET_r , the ET_rF and ET_{ins} values are not reported, because of the numerical instability caused during calibration by exponential increase of calibration coefficients a, b due to excess increment of ET_r , giving strong negative H values and large stability corrections.

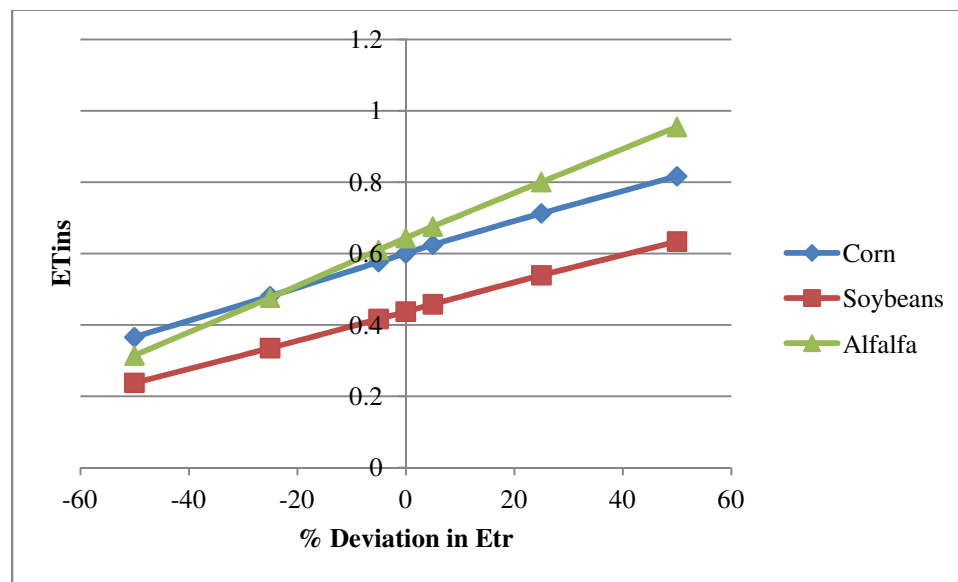


Figure 19: Instantaneous ET variations for September 27 2009 image

For September image (Figure 16), the curves are flat for soybeans and alfalfa. But for corn, the curve is not linear. Figure 19 shows the variations of average ET_{ins} for September. Alfalfa fields have the conditions close to that of the cold pixel. So, ET_{ins} is proportional to the ET_r . Even though the ET_{ins} curve for soybeans and corn is linear, they are not parallel to alfalfa, because the slope is proportional to ET_rF . So, the hypothesis is, with slightly different slope than alfalfa, the ET_rF curves shall be horizontal just like May and July images. Contradicting our hypothesis, the ET_rF curve for corn is not linear, and

unexpected rise in $ET_r F$ is found at -50% for both corn and soybeans. This sudden rise is because of the proportion of change in ET at warm pixels is lower than the cold pixels because of instability conditions raised for heat and momentum transport such that H increases and ET, drops down. So, when ET_r is reduced by 50%, the ET_{ins} at corn (warm pixels) decreases, such that it falls close to that of ET_r , which is evident from figure 19. So, $ET_r F$ values rises all the way up to K_c cold.

The strange behavior of corn curve is due to the fact that corn fields are filled with the stalks and stubble with low vegetation, and all the fields have low surface temperature close to the cold pixel. This may be due to harvesting or senescence.

In fully vegetated conditions, irrespective of the crop type, the $ET_r F$ is insensitive to ET_r . The change is less than 1% even though the change is 50%. But $ET_r F$ is found to be relatively sensitive to the bare soil conditions and can give unexpected values having biases up to 22% when ET_r is changed by 50%. But, ET_{ins} is sensitive to ET_r at vegetative fields, and the average error is found to be linear with error in ET_r and ET_{ins} is relatively insensitive to ET_r at bare soil fields. We can conclude that at full vegetated conditions, the $ET_r F$ values are consistent irrespective of the crop type and relatively sensitive at bare soil fields with changes in ET_r .

	$\partial ET_r F / \partial ET_r$		
Image month	Corn	Soybeans	Alfalfa
May	0.08/100%	0.05/100%	0.12/100%
July	~0.00/75%	~0.00/75%	0.06/75%
September	0.23/100%	0.07/100%	0.01/100%

Table 7: Absolute change in average $ET_r F$ when reference ET is changed, for all images considered.

Table 7 shows the absolute change in average ETrF when reference ET is changed globally from -50% to +50% for various months and different crop types.

3.2.5 Sensitivity towards Selecting Hot and Cold Pixels

Selecting the boundary pixels for model calibration is utmost important and highly sensitive and differs from user to user. In a sensitivity analysis on SEBAL by Wang et al. (2009), they found that selecting different hot and cold pixels leads to large deviations in final ET. So, in our analysis, different cold anchor pixels are selected such that they are warmer than the original cold pixel. In the same way, different hot anchor pixels are selected such that they are cooler than the original hot pixel. Our emphasis is on the temperature and land surface type primarily.

All the curves in this section are attained using, ETrF obtained at 15 randomly chosen pixels across the image, whose T_s varied from cold pixel temperature to hot pixel temperature, irrespective of the surface cover type. However, no water bodies are selected in this process.

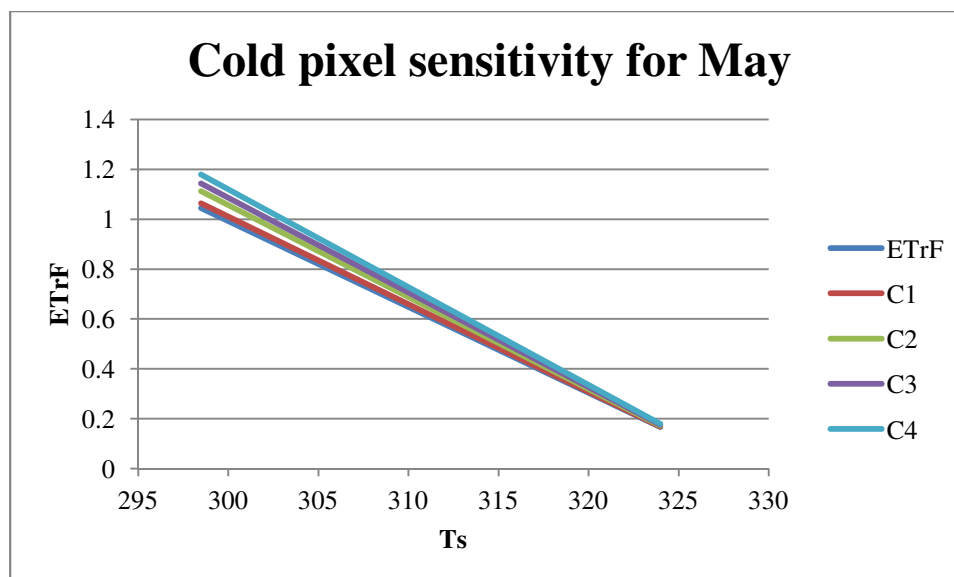


Figure 20: Sensitivity of the model to selection of cold pixels on May 30 2009. C1= 0.502K, C2= 1.002K, C3 = 1.996K, C4 = 3.005 K, ET_{rF} is base ET_{rF} with no change in original cold pixel temperature

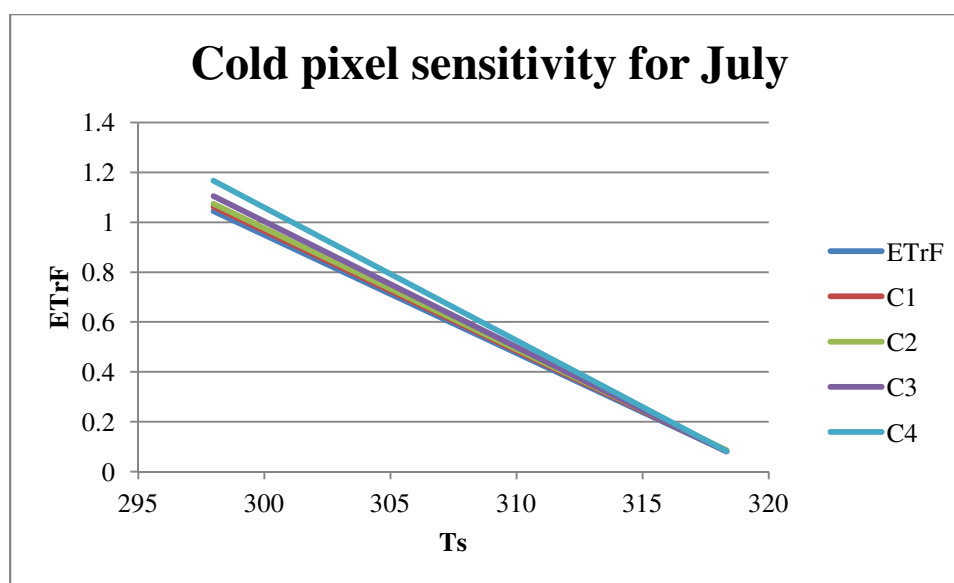


Figure 21: Sensitivity of the model to selection of cold pixels on July 1 2009. C1= 0.506K, C2= 1.010K, C3 = 2.012K, C4 = 3.006 K, ET_{rF} is base ET_{rF} with no change in original cold pixel temperature

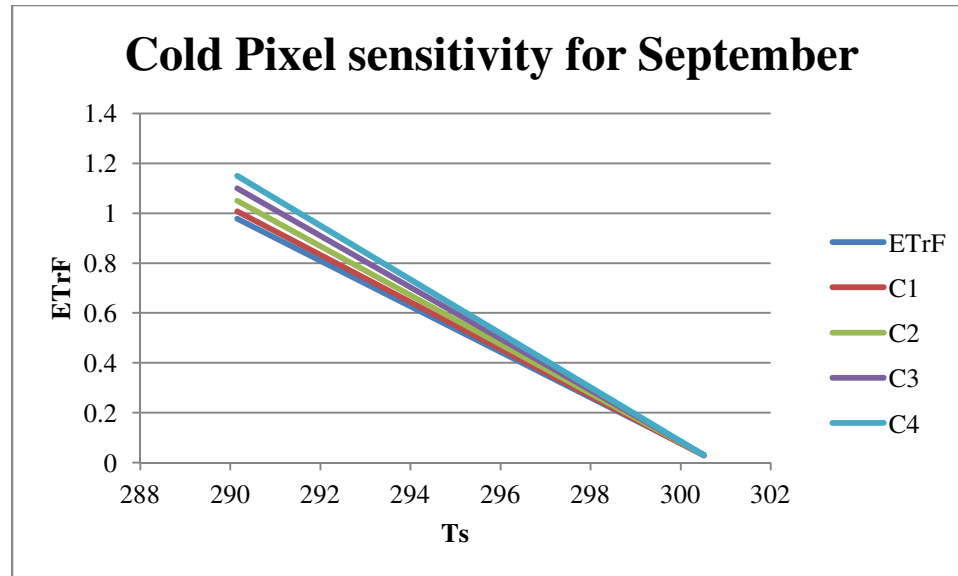


Figure 22: Sensitivity of the model to selection of cold pixels on September 27 2009. C1= 0.409K, C2= 1.047K, C3 = 2.085K, C4 = 2.866 K, ET_rF is base ET_rF with no change in original cold pixel temperature

Figures 20-22 show the sensitivity of ET_rF to the wide selection of different cold pixels for May, July, September images. C1, C2, C3, C4 represent the corresponding increase in temperature from the original cold pixel temperature. All the figures show ET_rF changes near the cold pixels and the curves converge towards the hot pixel side. This confirms the error in selection of cold pixel temperature effects most on the cold pixels and the effect diminishes as the temperature of pixels increases. Most change in ET_rF is noted at the coldest pixel and at maximum change in temperature, for all the images.

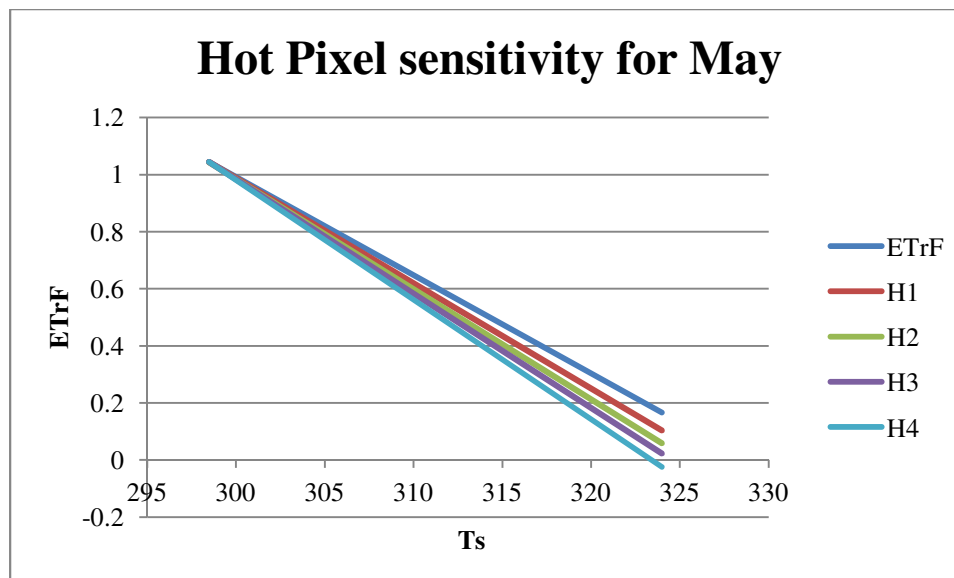


Figure 23: Sensitivity of the model to selection of hot pixels for May 30 2009. H1=- 0.427K, H2= -1.28K, H3 = -2.138K, H4 =- 3.029 K, E_{TrF} is base E_{TrF} with no change in original hot pixel temperature

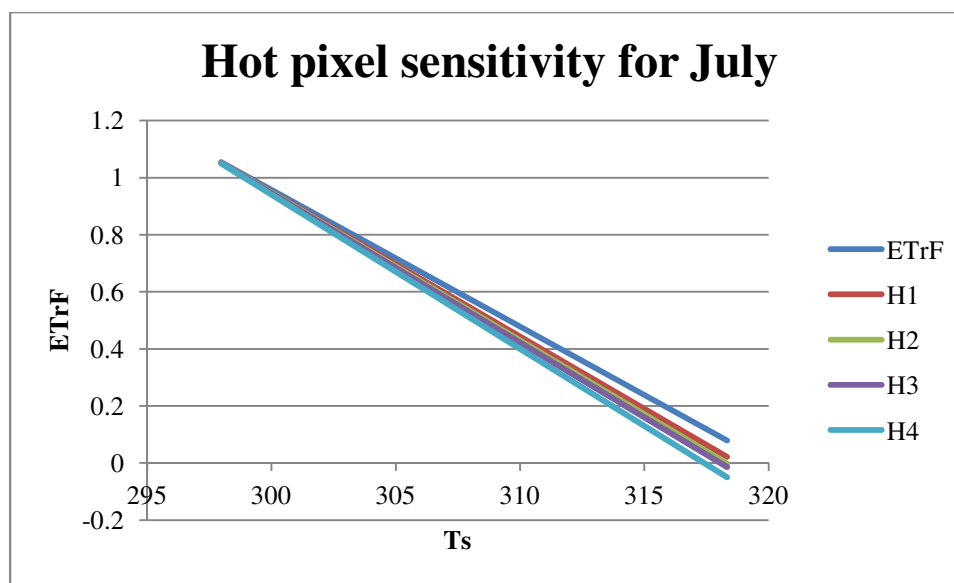


Figure 24: Sensitivity of the model to selection of hot pixels for July 1 2009. H1= -0.445K, H2= -0.886K, H3 = -1.771K, H4 = -3.11K, E_{TrF} is base E_{TrF} with no change in original hot pixel temperature

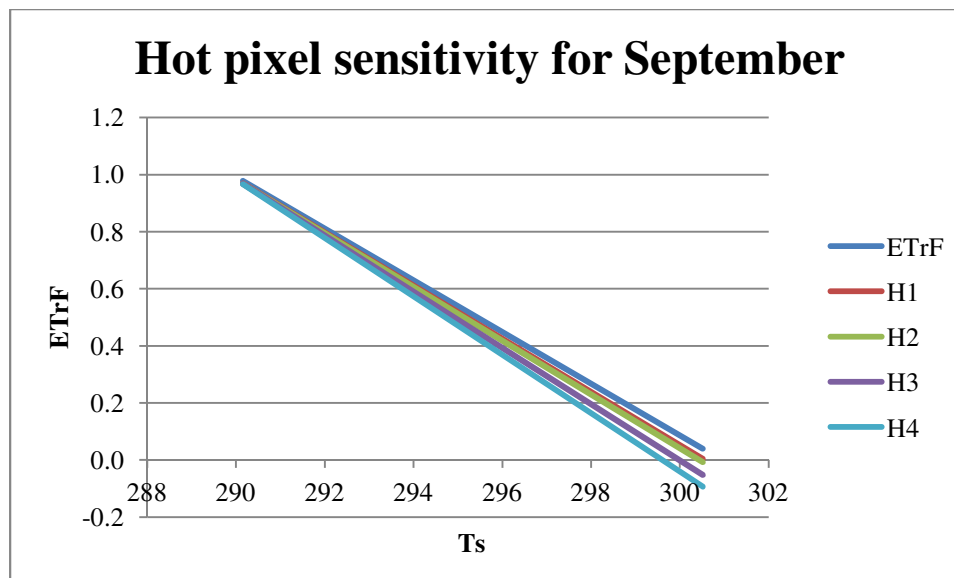


Figure 25: Sensitivity of the model to selection of hot pixels for September 27 2009. H1= -0.977K, H2= -0.995K, H3 =-1.958K, H4 = -2.962K, ET_{rF} is base ET_{rF} with no change in original hot pixel temperature

Figures 23- 25 show the fluctuations in ET_{rF} with selecting different hot pixels with different land surface temperature for May, July, September images. H1, H2, H3, H4 represent the corresponding decrement of hot pixel temperature from the original hot pixel temperature. Selecting cooler pixels than the original hot pixel results in disturbance of calibration coefficients, resulting in changes in ET. From the above figures it is evident that the ET values remains unchanged at cold pixels and maximum change at the hottest pixel and medium range pixels deviated medium. All the curves converge towards the cold pixel. Difference between H1 and H2 is less for September curves. So, they appeared to be overlapping. The author is unable to find the 0.5K difference in temperature pixels on the image. So, two pixels with minor difference in temperature are selected as H1, H2. From the above results, it is evident that the selection of hot pixels

has direct impact on ET assessment for bare soils or for water stressed areas and not sensitive to well watered vegetated surfaces.

	$\partial ET_r F / \partial T$	
	Sensitivity of cold pixel selection	Sensitivity of hot pixel selection
May	4%/K	-38%/K
July	3%/K	-54%/K
September	6%/K	-111%/K

Table 8: Maximum relative change in ETrF, when different hot and cold pixel temperatures are selected

Table 8 shows the maximum relative change in ETrF, when different hot and cold pixel temperatures are selected for May, July, September images.

Chapter 4: Local error

The estimation of ET through METRIC gave consistent results (from previous chapter) even bias exists in the input data. This chapter is mainly intended for behavior of the model to the local systematic errors which do not pass through the calibration. For this study, the parameters estimated empirically are considered. Even though the biases in input data and other empirically estimated parameters may affect the output ET, the scope of this study is limited only to albedo α , soil heat flux G , Momentum roughness length Z_{om} , Surface temperature T_s , Difference between air and surface temperature dT . These are primary parameters affecting the computation of ET in METRIC and generally have the greatest uncertainty in estimation for specific land cover or vegetation type or amount.

4.1 Methodology

In local error, the error is not mitigated through calibration. Sensitivity of albedo, soil heat flux, Difference between air and surface temperature to the final ET_rF estimates is done by varying the respective variables at a range of -50% to +50%. Surface temperature is varied from -2K to + 2K and momentum roughness length is doubled and halved (Tasumi 2003). Absolute values are used for surface temperature and momentum roughness length and relative values are used for the remaining parameters. T_s is varied as : T_s-2 , T_s-1 , $T_s-0.5$, T_s , T_s+1 , T_s+2 , T_s+3 . Z_{om} is varied as: $2 * Z_{om}$ and $0.5 * Z_{om}$. Where T_s , Z_{om} are the base values of surface temperature and momentum roughness length. Whereas for remaining parameters their base values are deviated as: 1.5X, 1.25X, 1.05X, 0.95X, 0.75X, 0.5X. Where X is the respective base values. These changes were made to

all pixels in the image, but after calibration of METRIC to the image. The changes represent deviations or uncertainties in estimates for parameters that might occur for specific pixels or land covers that are not globally systematic and accounted for during calibration of the overall image.

4.2 Results and Discussions

All the curves presented in the following sections are average curves of all 14 fields for each crop type. The error bars in the figures describe the maximum and minimum values of ET_rF for each crop type.

4.2.1 Albedo (α)

In METRIC, albedo is calculated using the following equation.

$$\alpha = \sum_{b=1}^{b=6} \rho_b \cdot w_b$$

Where ρ_b is reflectance at surface at band b and w_b is weighting coefficient at band b. These weighting coefficients are obtained by the ratio of at surface hemispherical solar radiation at that particular band to the at surface hemispherical solar radiation over the entire solar spectrum (0.3-4.0 μm) (Starks et al. 1991) and band 6, in this equation is Landsat's band 7. The weighting coefficients proposed are for low haze atmospheric conditions by Tasumi et al. (2008). The coefficients differ slightly for extremely transparent atmosphere and low transmittant atmosphere. Albedo comparisons were done with the work done by Liang (2000) and observed a random deviation for extremely bright surfaces.

Canopy structure shading (Li et al. 1992; Leblon et al. 1996; Ekstrand 1996), shadows casted by the nearby objects (Teillet et al. 2001; Starks et al. 1991) can cause errors in reflectance by directly affecting the albedo. In addition, the near nadir-view of Landsat can cause albedo of tall crops like corn or crops with vertical leaf structure like wheat to be estimated lower than the true hemispherical albedo due to impacts of shadows deep in the canopies that are viewed by nadir and that carry too much weight in the albedo estimation (Allen et al. 2011, pers. Commun. (paper in preparation)). When the sun and sensor angles match, canopy reflectance can be large (hotspot). These hotspots can overestimate albedo by 20%. Conversely, when solar angle is substantially different from the sensor view angle, albedo can be less than hemispherical albedo. This phenomenon is known as bidirectional reflectance distribution function (BRDF) and is corrected for in MODIS-based albedo retrievals (Gao et al. 2005, Salomon et al. 2006) but not for Landsat. Also, the extrapolation of reflectance to the nearby bands can also be possible source of error in estimating albedo (Starks et al. 1991). The effects of various tillage practices on albedo are considerable. Typical tillage systems decreases the albedo up to 25% when soil is moist and about 12% when soil is dry (Oguntunde et al. 2006). Even though the weighting coefficients proposed by Tasumi et al. (2008) are optimized for Landsat images, this study is done to observe the behavior of METRIC model to biases in estimating albedo.

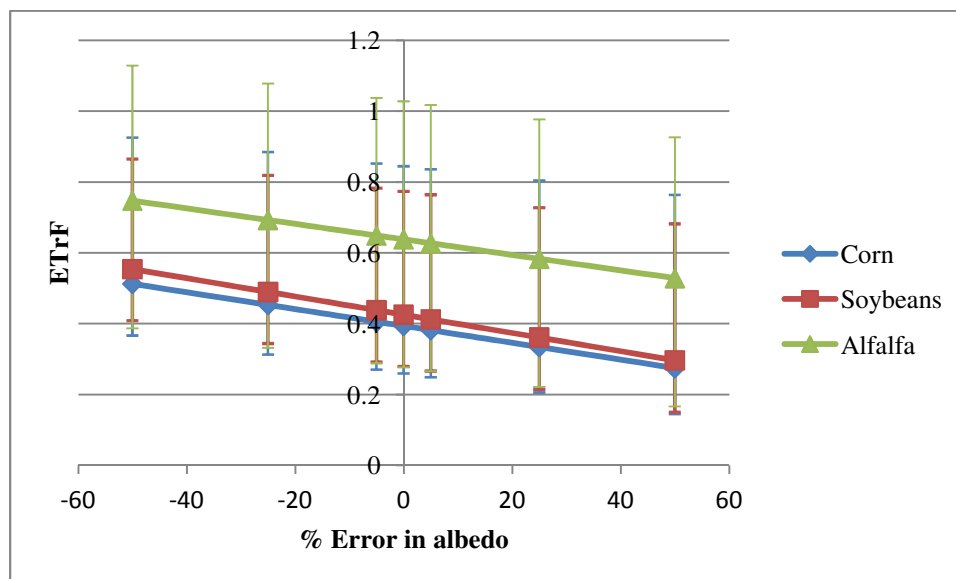


Figure 26: METRIC's local sensitivity to albedo for May image

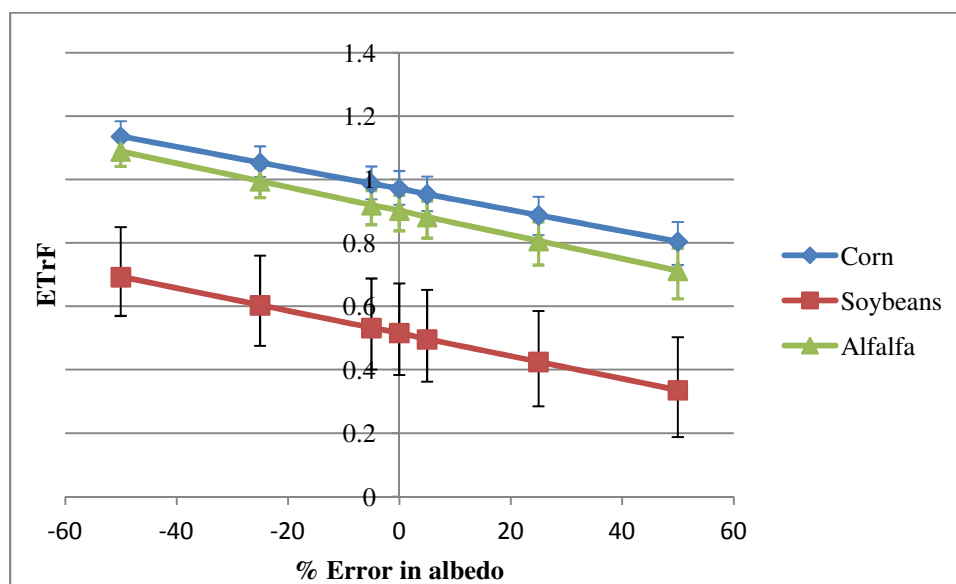


Figure 27: METRIC's local sensitivity to albedo for July image

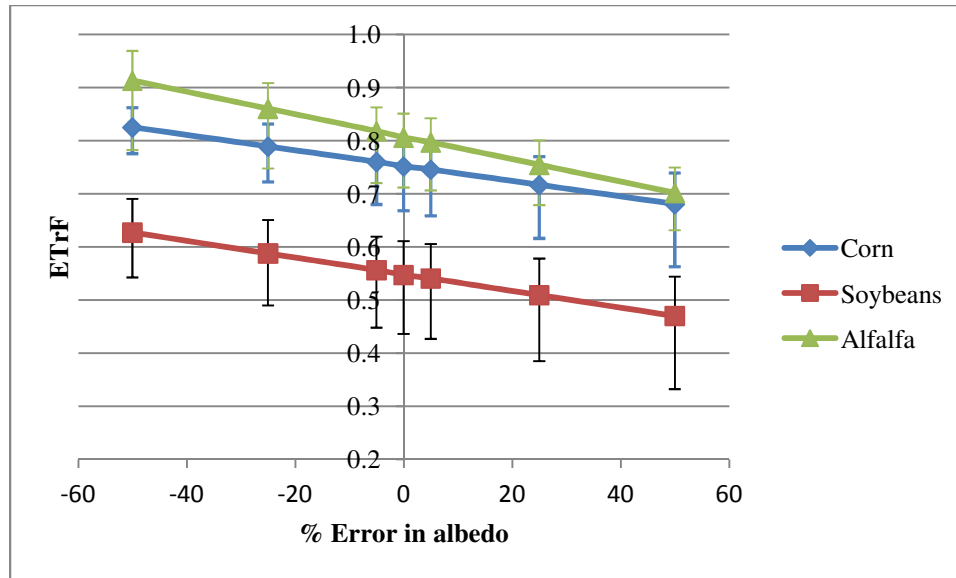


Figure 28: METRIC's local sensitivity to albedo for September image

Image date	$\partial ET_r F / \partial \alpha$		
	Corn	Soybeans	Alfalfa
May	-0.24/100%	-0.26/100%	-0.22/100%
July	-0.33/100%	-0.36/100%	-0.38/100%
September	-0.14/100%	-0.16/100%	-0.21/100%

Table 9: Maximum absolute change in average ETrF when albedo is changed

Figures 26- 28 show the model's local sensitivity to albedo. For all the seasons and for all crop types, $ET_r F$ increased, with decrease in albedo and decreased with increase in albedo. With increase in albedo the outgoing shortwave radiation increases and the net radiation decreases, through which the available energy for evapotranspiration decreases, so decreased $ET_r F$ values and vice versa.

For only September image, the corn curve has different slope than the other curves. This is because of low albedo for corn, so that the change in albedo was smaller

and therefore impact on ET_rF is less. The average albedos for September image are 0.178 and 0.122 for alfalfa and corn respectively. At 50% change in albedo, variations in alfalfa are large compared to that of corn. So, large deviations are seen for alfalfa in September than the other images where the differences in average albedos are small (Table 1).

Above Figures show the average ET_rF values for 14 different fields of each crop type. The error bars for each plot indicate the minimum and maximum values of all the fourteen fields.

Table 9 shows the maximum absolute change in average ET_rF when albedo is changed at a local scale from -50% to +50% for various months and different crop types.

4.2.2 Soil heat flux (G)

Soil heat flux is a complex phenomenon, which depends upon various factors like soil type, moisture content, cracking, delamination, mineral content etc. It is difficult to get an accurate estimate, particularly in regional scale. Choudhury et al. (1987) emphasized on accurate estimation of G and its relation in estimation of ET .

De Bruin and Holtslag (1982) used G/R_n ratio as 0.1 for short grass land cover type and found the bias in G up to 50% of the calculated value. Clothier et al. (1986) observed a standard error of 21.6% in estimating mean G/R_n ratio for alfalfa when related to height of the alfalfa crop. Kustas and Daughtry (1990) confirmed the results of Clothier et al. (1986) with slight deviation caused by different soil conditions and different vegetation types. Choudhury et al. (1987) related G/R_n with LAI and reported correlation coefficient of 0.97 for nine days combined.

In METRIC soil heat flux G is calculated using empirical equation proposed by Tasumi (2003), G/R_n as a function of leaf area index (LAI) for vegetated surfaces and function of surface temperature for bare soils (but these equations may not be applicable to non agricultural soils). LAI varies with canopy structure and plant row width (Wall et al. 1990). For two different crops having same NDVI, may not have same LAI, which may result bias in estimating LAI and G . LAI is calculated empirically from soil adjusted vegetation index (SAVI). Allen et al. (2007a) proposed, to compute SAVI using local calibration.

If SAVI for a pixel is miscalculated as 0.65 instead of 0.7, then the percentage error in calculation of LAI is around 20%, because $LAI = 11(SAVI^3)$ if $SAVI < 0.817$. This 20% error in LAI can lead up to 16% error in estimating G . Apart from empirical relations, due to errors in the satellite input data (see previous chapter) might have biases in estimating R_n through G . Even though the contribution of global systematic error in G has little effect on the final ET values (Allen et al. 2007a), this study is done to observe the effect of local systematic error in G on final ET product.

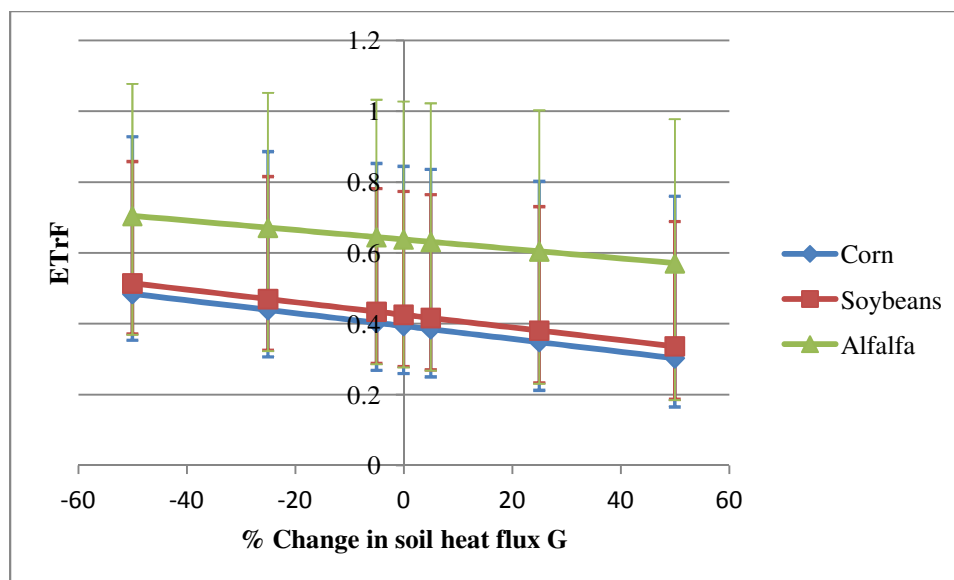


Figure 29: Model response to variations in G for May image

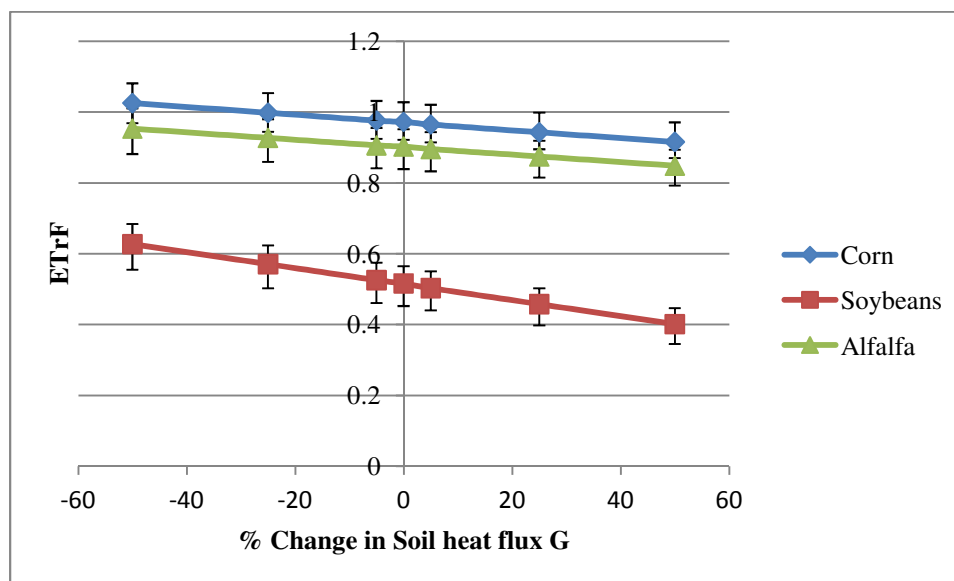


Figure 30: Model response to variations in G for July image

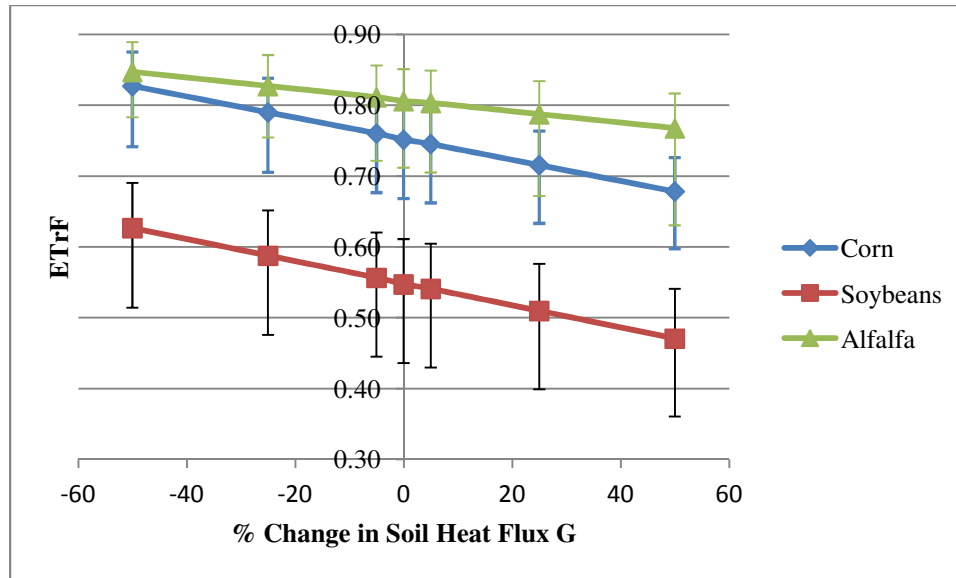


Figure 31: Model response to variations in G for September image

Image date	$\partial ET_r F / \partial G$		
	Corn	Soybeans	Alfalfa
May	0.18/100%	0.18/100%	0.13/100%
July	0.11/100%	0.23/100%	0.11/100%
September	0.15/100%	0.16/100%	0.08/100%

Table 10: Maximum absolute change in average ETrF when soil heat flux is changed

Figures 29- 31 show the variations in $ET_r F$ with change in soil heat flux G for May, July and September images. Our hypothesis is, increase in soil heat flux leads to decrease in ET because the available energy decreases, as R_n , H remains constant for this local error in G. The same discussion applies vice versa. For all the image dates, and all the crop types, the results are as hypothesized.

The slopes for each crop type are different for different images. This is because, of different field conditions. For bare soil conditions, G is more than that of vegetative

conditions. Because the deviations are applied on base values, the deviations are more pronounced in bare soil or less vegetative conditions. So, the fields having bare soil conditions have more slope than the vegetative conditions, whose slope is relatively small.

The site conditions in May, for Corn and Soybeans are similar. The maximum NDVI of corn and soybeans are 0.31 and 0.27 respectively. And the surface temperature is same. All the corn and soybean fields are bare soil in nature in May. The selected alfalfa fields have wide variety of vegetative conditions in May. The minimum, maximum and average NDVI of alfalfa fields are 0.23, 0.82 and 0.52. So, the behavior of alfalfa curve in May is slightly different from corn and soybeans.

In July image, the soybean fields have a maximum NDVI of 0.64. So, soybean fields have less vegetation, whereas, corn and alfalfa has more vegetative cover. So, the curves of corn and alfalfa have less slope than soybeans. In September, except alfalfa, the remaining two crop types have more exposed bare soil in general (From NDVI values of table 1). So, the soybeans and corn curves are parallel and have steeper slopes than slope of alfalfa.

Table 10 shows the maximum absolute change in average ETrF when soil heat flux is changed at a local scale from -50% to +50% for various months and different crop types.

4.2.3 Momentum roughness length Z_{om}

At height of $d+Z_{om}$ the wind speed extrapolates to zero. Where d is zero plane displacement. Momentum roughness length is a measure of roughness of the layer that interacts with the surface. The more the Z_{om} , the rougher is the surface and vice versa. Brutsaert (1982) empirically related Z_{om} to the crop height. Tasumi (2003) related Z_{om} with LAI as

$$Z_{om} = 0.018 \times LAI$$

Verhoef et al. (1997) compared Raupach (1992), Raupach (1994) models with the literature values for sparse canopies and found the later model gave better results with simple equation. Tian et al. (2011) tested four models (Choudhury & Monteith, 1988; Raupach 1994; Schaudt & Dickinson 2000; Nakai et al. 2008) and found Schaudt & Dickinson model which uses LAI and FAI (frontal area index), gave a better estimate of Z_{om} .

In METRIC, Z_{om} is calculated using land use map. For non agricultural areas, Z_{om} is assigned the values given by Tasumi (2003). For agricultural areas, Z_{om} is calculated using above equation. When land use map is not available, Z_{om} is a function of NDVI (Bastiaanssen, 2000) or NDVI and albedo (Allen, 2002) or as a constant value for some landuses. Current METRIC applications use Perrier (1977) function to estimate roughness for trees (METRIC user manual 2011). In this study sensitivity analysis is done on Z_{om} calculated using land use map.

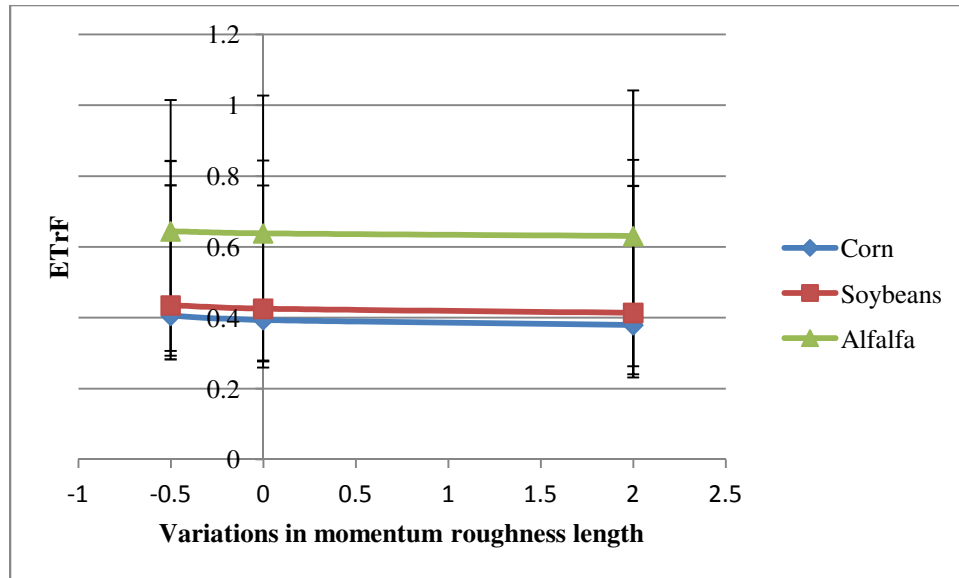


Figure 32: Change in ET with variations in Z_{om} for May image

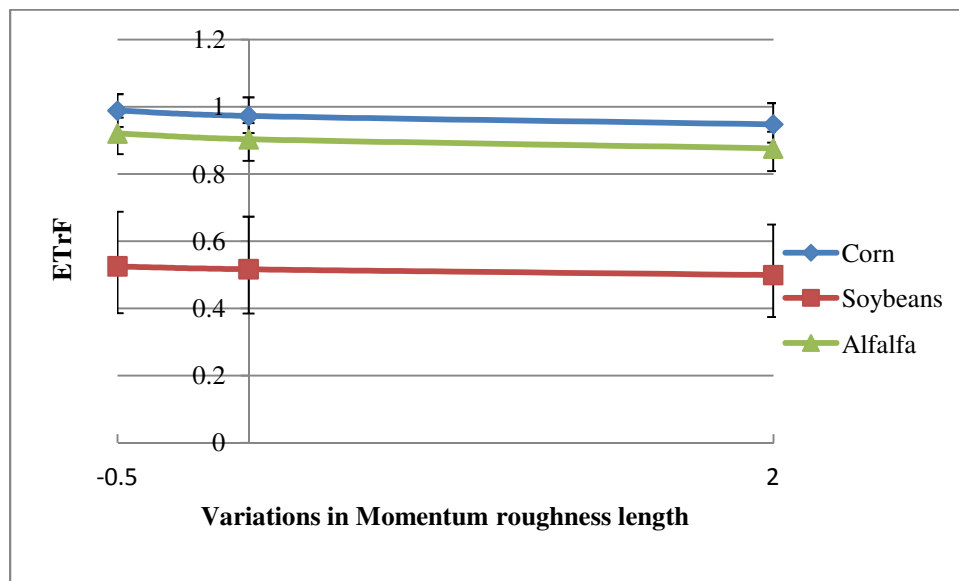


Figure 33: Change in ET with variations in Z_{om} for July image

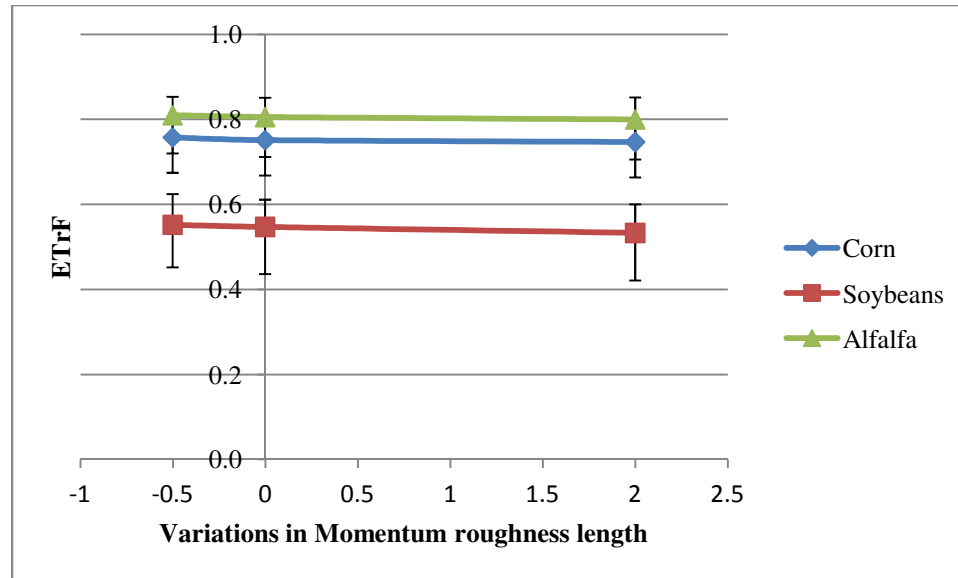


Figure 34: Change in ET with variations in Z_{om} for September image

According to our hypothesis, as the momentum roughness length increases, friction velocity increases through which resistance to heat transport decreases and thereby increase in H and decrement in ET can be observed. Applying this argument in reverse way, the ET increases, with decrease in momentum roughness length.

Figures 32-34 show the change in ET_rF with variations in Z_{om} . As, hypothesized, for all crop types and for all image dates, the ET_rF increased, with decrease in Z_{om} , and decreased with increase in Z_{om} . But, the increments and decrements are not significant because, numerically, Z_{om} is very less than the blending height 200 metres. Even doubling the original Z_{om} does not have significant affect in calculation of friction velocity and resistance to heat transport r_{ah} . So, relative change in ET is insignificant. The maximum change in average ET_rF is 0.04, for 150% change in Z_{om} (table 11).

	$\partial ET_r F / \partial(Zom)$		
Image date	Corn	Soybeans	Alfalfa
May	0.03/150%	0.02/150%	0.01/150%
July	0.04/150%	0.03/150%	0.04/150%
September	0.01/150%	0.02/150%	0.01/150%

Table 11: Maximum absolute change in average ETrF when momentum roughness length is changed

Table 11 shows the maximum absolute change in average ETrF when momentum roughness length is changed at a local scale from -50% to +100% for various months and different crop types.

4.2.4 Near surface temperature difference dT

dT is the temperature difference at heights z_1, z_2 . In METRIC z_1 is 0.1m and z_2 is 2 m. However, temperature data at heights z_1, z_2 is unknown for each pixel. The individual temperatures at 0.1m and 2m are not necessary, because dT alone is needed for computation of sensible heat flux H. Previous research results showed that dT is linearly related to radiometric surface temperature (Wang et al. 1995, Jacob et al. 2002). In METRIC, dT is related to surface temperature as:

$$dT = aT_s + b$$

Where a and b are correlation coefficients obtained by selecting hot and cold pixels on the image, and by iteration process, until rah and dT are stabilized at the hot pixel (See previous chapter).

Watts et al. (2000) used Chehbouni et al. (1996, 1997) equation of relating the difference of aerodynamic surface temperature and air temperature with radiometric surface temperature and air temperature with an empirical function of LAI and found an

r^2 value of 0.9 when comparison was made between simulated and eddy flux calculated sensible heat flux. Xu et al. (2008) found large deviations in calculation of sensible heat flux when air temperature is treated as constant, obtained from nearest weather station. Marx et al. (2008) computed the maximum relative uncertainty of estimating sensible heat flux using SEBAL (Bastiaanssen et al. 1998) as 20% over savannah environment.

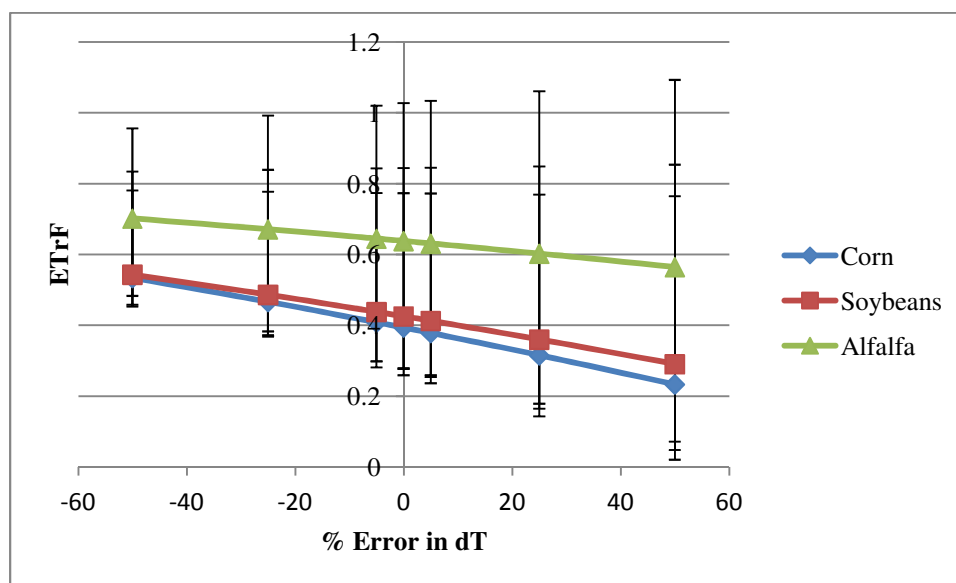


Figure 35: Changes in ET_rF with error in dT for May image

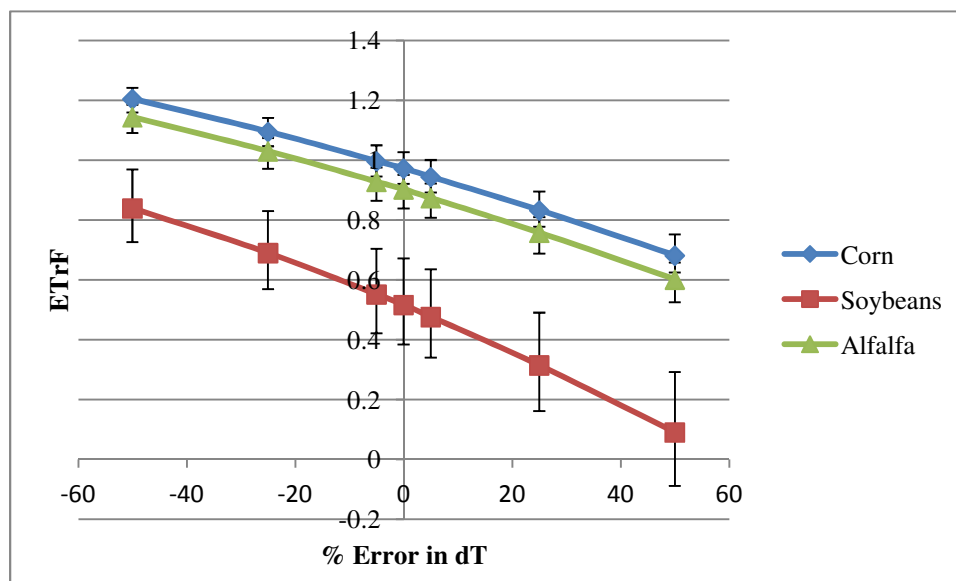
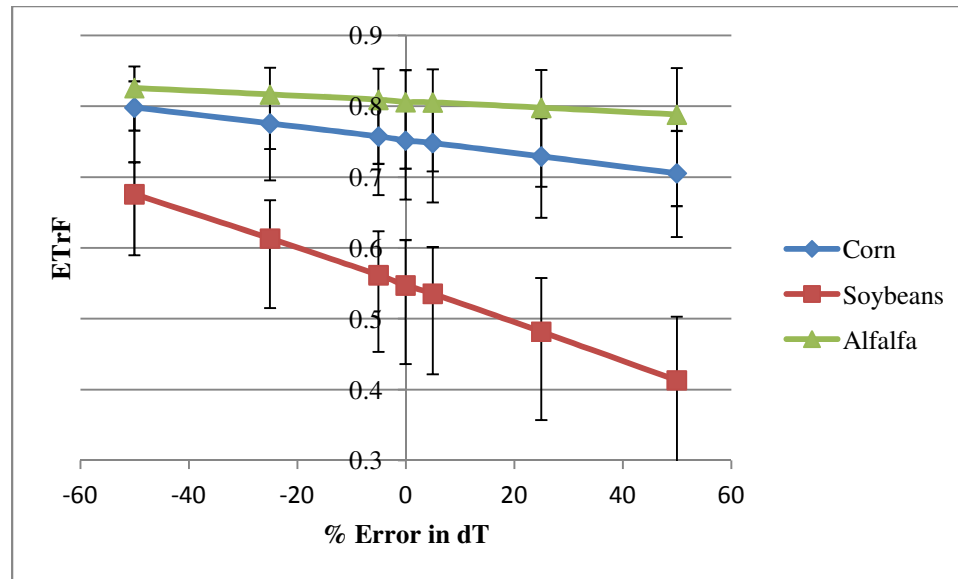


Figure 36: Changes in ET_rF with error in dT for July image**Figure 37:** Changes in ET_rF with error in dT for September image

The difference between air and surface temperature is calculated empirically using calibration constants; the hot pixels have more dT than that of cold pixels. Our hypothesis is that, with increase in dT , increment in H is expected, and the residual energy for ET decreases. With decrement in dT , increment in ET is expected. Since, the change in dT is relative, the deviation in ET curves for bare soil fields is more than the deviation of ET curves in vegetated fields.

Figures 35- 37 show the changes in ET_rF with percentage error in dT . For all the fields and all the crop types, the curves are as hypothesized. But, change in the ranges for all crop types, for all the images is observed except for corn and alfalfa in July image. This is because of the variations in range in dT . When dT is increased, the increment in dT for warm pixels is higher than the cold pixels. So, the range of dT for warm pixels increases. When dT is decreased, the decrement is more pronounced in warm pixels, so,

the range of dT falls in the region of cold pixels. Since, the change in dT for cold pixels is less, the change in ET_rF is also less. The range variations can be observed only for the crops having the mixed field conditions.

In May, alfalfa fields have more vegetation than corn and soybean fields. So, the response ET curves have smaller slope than corn and soybeans. The average surface temperature of corn is slightly higher than soybeans (see the table). So, the ET curve for corn is slightly different from soybean curve. As discussed earlier, the range of dT decreased, as dT is decreased, so, the ET_rF values coincide each other for corn and alfalfa. For July image, the corn and alfalfa are parallel to each other, with no range variations; this is because all the fields of corn and soybeans have vegetation and soybeans have mixed field conditions, so range variations can be observed.

In the September image, for alfalfa, the ET_rF curve is relatively flatter than the other curves, because most of the alfalfa fields have full vegetation cover and low surface temperatures. The soybean curves have higher slope than that of corn because the soybean fields have higher surface temperatures than corn. Corn has bare soil conditions, but with lesser temperature than soybeans. So, the slope of the corn curves is more than that of alfalfa and less than that of soybeans. It is noted that these ranges in error for dT ($\pm 50\%$) are unreasonable since it is recognized that the calibration of METRIC will nearly always be much less than 50% from the proper values (unless a major coding error occurs). Therefore, the dT vs. T_s function will estimate dT for any specific pixel well within 50% of the true value of dT required to accurately estimate H .

	$\partial ET_r F / \partial (dT)$		
Image date	Corn	Soybeans	Alfalfa
May	0.30/100%	0.25/100%	0.14/100%
July	0.52/100%	0.75/100%	0.54/100%
September	0.09/100%	0.26/100%	0.04/100%

Table 12: Maximum absolute change in average ETrF when dT is changed

Table 12 shows the maximum absolute change in average ETrF when dT is changed at a local scale from -50% to +50% for various months and different crop types.

4.2.5 Surface temperature T_s

Surface temperature in METRIC follows the plank equation where the correction to thermal radiance is calculated using Wukelic et al. (1989). Li et al. (2004) found mean absolute difference in estimating surface temperature for Landsat 7 is 0.98 K, Landsat 5 is 1.47 K when compared with tower measurements. Gillespie et al. (1998) with proper atmospheric correction attained the accuracies in temperature estimation about ± 1.5 K. The spatial resolution of thermal band in Landsat TM/ETM, errors in image geo referencing (Li et al. 2004), improper atmospheric correction (Li et al. 2004 & Gillespie et al. 1998), precision, calibration, empirical relationships, (Gillespie et al. 1998) are the sources of errors in estimating the radiometric surface temperature.

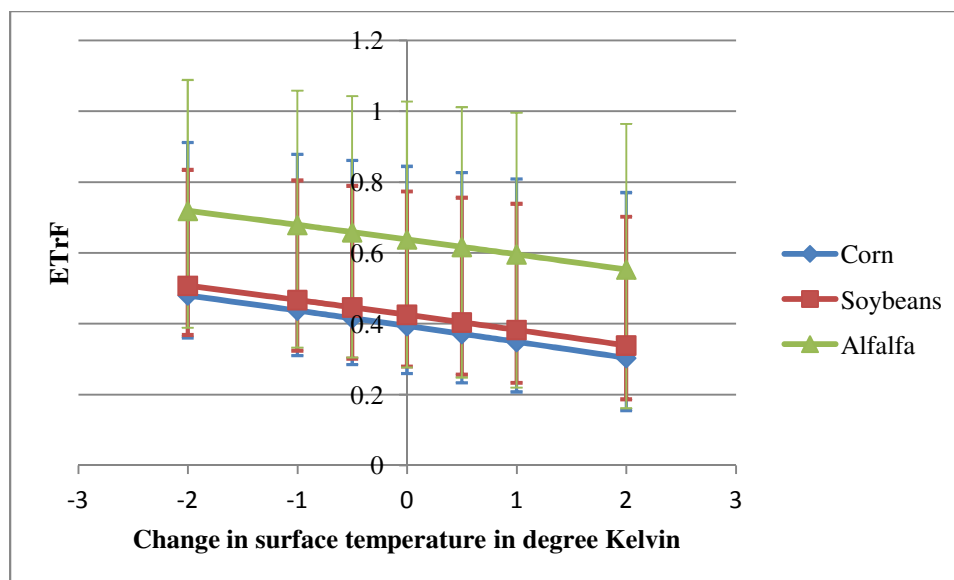


Figure 38: Model's response to change in local T_s for May image

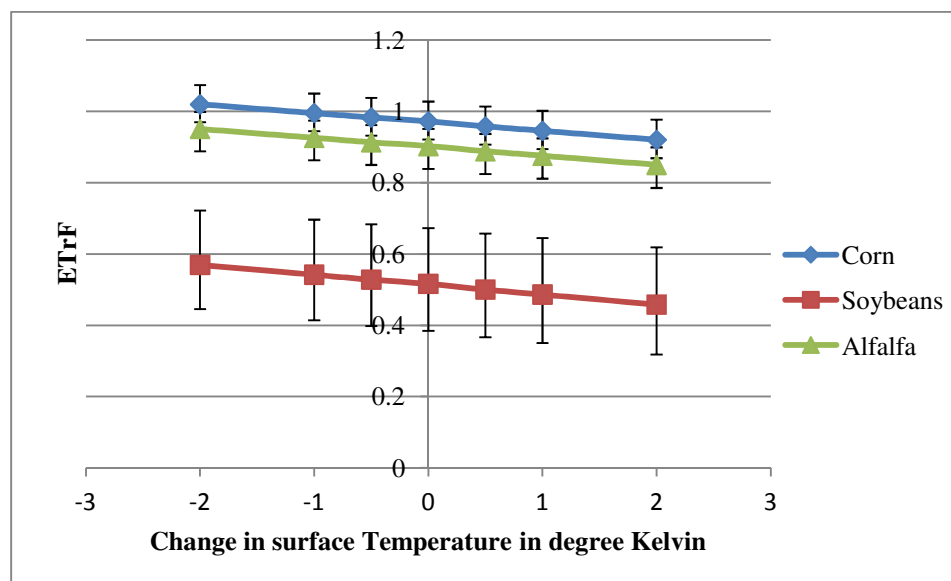


Figure 39: Model's response to change in local T_s for July image

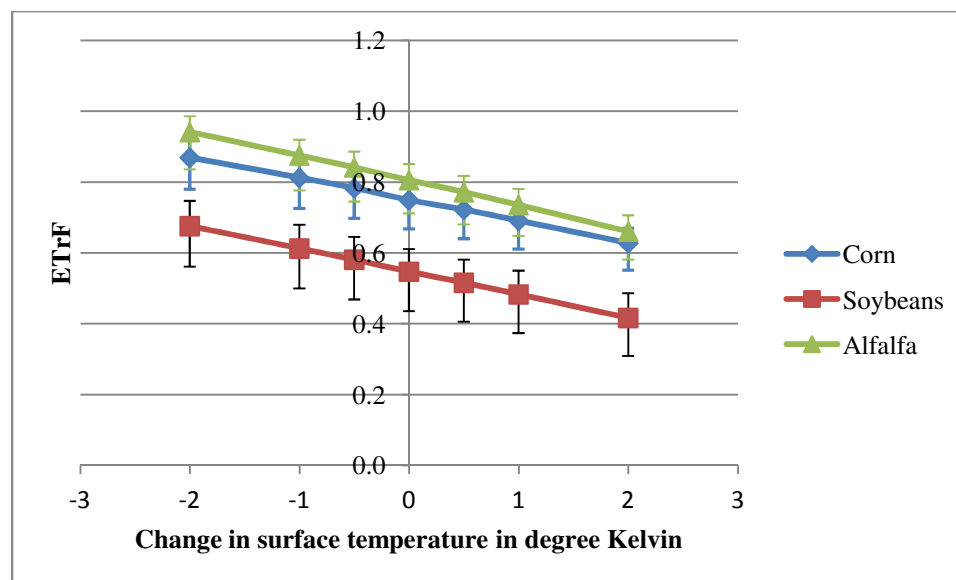


Figure 40: Model's response to change in local T_s for September image

The hypothesis is, with increase in surface temperature, the sensible heat flux increases, because H is directly proportional to a , b (dT) which are fixed for each image and is a function of surface temperature. Even though the net long wave radiation is a function of surface temperature, during day time, the effect of net long wave radiation is smaller than the short wave radiation. So, the change in net long wave radiation with 2K change in surface temperature can be ignored. So, with increase in surface temperature, the residual energy for latent heat flux decreases, so, decrement in ET_rF can be expected. With decrement in surface temperature, increment in ET_rF can be hypothesized.

Figures 38- 40 show the METRIC's behavior to local error in surface temperature for corn, soybeans and alfalfa in May, July and September images. Response curves for all crops for all the images are well in agreement with our hypothesis. For all the images, the curves are parallel to each other. Not only the average values, but the behavior of all pixels is similar, which is evident from the maximum and minimum limit bars of each

crop type. Since, the change in surface temperature is absolute, the response for all crop types are similar for each image. If relative change is made, the hot pixels like bare soil areas would have more slope than the cold pixels like vegetative surfaces.

	$\partial ET_r F / \partial T_s$		
Image date	Corn	Soybeans	Alfalfa
May	0.18/4°K	0.17/4°K	0.17/4°K
July	0.10/4°K	0.11/4°K	0.10/4°K
September	0.24/4°K	0.26/4°K	0.28/4°K

Table 13: Maximum absolute change in average ETrF when surface temperature is changed at local scale

Table 13 shows the maximum absolute change in average ETrF when surface temperature is changed at a local scale from -50% to +50% for various months and different crop types.

Chapter 5: Conclusions

Calibration is the most crucial part in this model. METRIC has the capability of producing consistent results if calibration is done well. METRIC produces stable results even though the input data has large deviations. On the other hand, model is sensitive to input parameters if calibration process goes wrong. Maximum error observed due to $\pm 50\%$ deviation in reflectance, incoming long wave radiation, reference evapotranspiration, wind speed is 16%, 46%, 60%, 11% of the original ET_rF .

	$\% \partial ET_rF / \partial(\text{parameter})$								
% Error	May			July			September		
Variables	Corn	Soybeans	Alfalfa	Corn	Soybeans	Alfalfa	Corn	Soybeans	Alfalfa
ρ	9	17	1	0.6	3	5	3	7	6
τ	1	1	1	1	4	2	3	2	3
T_s	0.6	0.6	0.3	0.2	0.6	0.2	0.8	0.2	0.3
ET_r	13	8	11	0.5	4	5	22	8	2
u	8	7	5	0.9	7	2	4	6	3
Cold Pixel selection	13			12			18		
Hot pixel Selection	115			163			335		

Table 14: Percentage change in ET_rF when each parameter is changed to its extreme limit on one side for May, July, September images: Global Error.

Table 14 shows the maximum average error in ET_rF to each parameter, when it is changed to its extreme limit on one side, for each image, for each crop type. From above

table and figures, we can conclude that the variables reflectance, transmittance, surface temperature, wind speed are less sensitive than the other parameters as the errors lie within 10% even though the base values are changed up to $\pm 50\%$. Wind speed accuracy should be maintained, as wind speed below a certain limit can cause numerical instability in METRIC for calibration. Errors induced by deviation in ET_r are within 5% if the surface has vegetation at full extent. The error can vary up to 22% for bare soil conditions when ET_r is reduced by 50% of its base value. Also, over estimate of ET_r can cause errors due to numerical instability in calibration process. So, care should be taken to ensure the quality of weather station is good.

Selection of hot and cold pixels is most prone to errors (J Wang et al., 2009) and is not currently automated. Variations in ET are high at warm pixels when selecting different hot pixels and variations are seen at cool pixels when selecting different cold pixels. So, from the table we can conclude that selection of hot cold pixels is highly sensitive to the final product of the model.

The local error analysis is performed on albedo, soil heat flux, surface temperature, Difference between surface and air temperature and momentum roughness length for May (Landsat 5), July (Landsat 5), September (Landsat 7) images. For this analysis, the model is pre calibrated and the calibration constants a, b are not changed for each model's run. The constants a, b are obtained when the images were run on natural conditions without altering any variable.

The maximum change in average of 14 fields ET_rF for May, June, September images for various parameters at their extreme limits are given in the following table 15.

	$\% \partial ETrF / \partial(\text{parameter})$								
% Error	May			July			September		
Variables	Corn	Soybeans	Alfalfa	Corn	Soybeans	Alfalfa	Corn	Soybeans	Alfalfa
α	30.2	30.2	17.2	17.2	35	21	9.7	14.5	13.3
G	23	20.8	10.4	5.82	22.2	6	10	14.5	5.1
T_s	22.9	20.3	13.2	5.3	11.2	5.8	16.2	23.8	18
dT	40.7	31.67	11.5	30	82.5	33.3	6.2	24.5	2.5
Z_{om}	3.6	2.6	1.1	2.6	3.4	3	0.8	2.5	0.7

Table 15: Percentage change in ETrF when each parameter is changed to its extreme limit on one side for May, July, September images: Local Error

From the table 15, we can conclude that care has to be taken while calculating dT, especially when hot pixels are dominating the image. For May, September images, alfalfa fields have more vegetation than corn and Soybeans whereas corn and soybeans have almost bare soil conditions. So, except for albedo, variations in the remaining parameters show the maximum deviation in corn and soybeans than that of alfalfa. In July Corn has more vegetative fields and low average temperature than that of alfalfa. So, minimum errors are observed in corn and alfalfa than in soybeans which has most of the fields with bare soil conditions. From this we can conclude that the model is relatively insensitive to vegetated surfaces, than the bare soil conditions for local errors.

More comprehensive research has to be done on various unconsidered parameters and interactive affects of multiple parameters, to observe the models response. Also, selection of hot and cold pixels should be automated, to get consistent results, from user to user.

References

Allen, R. G. (2002). "Evapotranspiration for southwest Florida from satellite-based energy balance." Rep. Prepared for Tampa Bay Water, Tampa Bay, Fla.

Allen, R. G. (2005). The ASCE standardized reference evapotranspiration equation, American society of civil engineers.

Allen, R. G., L. S. Pereira, et al. (1998). "Crop evapotranspiration-Guidelines for computing crop water requirements-FAO Irrigation and drainage paper 56." FAO, Rome 300.

Allen, R. G., M. Tasumi, et al. (2007a). "Satellite-based energy balance for mapping evapotranspiration with internalized calibration (METRIC)—Model." *Journal of Irrigation and Drainage Engineering* 133: 380.

Allen, R. G., M. Tasumi, et al. (2007b). "Satellite-based energy balance for mapping evapotranspiration with internalized calibration (METRIC)—Applications." *Journal of Irrigation and Drainage Engineering* 133: 395.

Bailey, W. G. and J. A. Davies (1981). "The effect of uncertainty in aerodynamic resistance on evaporation estimates from the combination model." *Boundary-Layer Meteorology* 20(2): 187-199.

Bastiaanssen, W. G. M., M. Menenti, et al. (1998). "A remote sensing surface energy balance algorithm for land (SEBAL). 1. Formulation." *Journal of Hydrology* 212: 198-212.

Bastiaanssen, W. G. M. (2000). "SEBAL-based sensible and latent heat fluxes in the irrigated Gediz Basin, Turkey." *Journal of Hydrology* 229(1-2): 87-100.

Brutsaert, W. (1982). *Evaporation into the atmosphere: Theory, history, and applications*, Springer.

Brutsaert, W. (1999). "Aspects of bulk atmospheric boundary layer similarity under free-convective conditions." *Reviews of Geophysics* 37(4): 439-451.

Chameides, W. L., H. Yu, et al. (1999). "Case study of the effects of atmospheric aerosols and regional haze on agriculture: An opportunity to enhance crop yields in China through emission controls?" *Proceedings of the National Academy of Sciences of the United States of America* 96(24): 13626.

Chehbouni, A., D. Lo Seen, et al. (1997). "Estimation of sensible heat flux over sparsely vegetated surfaces." *Journal of Hydrology* 188-189: 855-868.

Chehbouni, A., D. Lo Seen, et al. (1996). "Examination of the difference between radiative and aerodynamic surface temperatures over sparsely vegetated surfaces." *Remote Sensing of Environment* 58(2): 177-186.

Choudhury, B. J., S. B. Idso, et al. (1987). "Analysis of an empirical model for soil heat flux under a growing wheat crop for estimating evaporation by an infrared-temperature based energy balance equation." *Agricultural and Forest Meteorology* 39(4): 283-297.

Choudhury, B. J. and J. L. Monteith (1988). "A four layer model for the heat budget of homogeneous land surfaces." *Quarterly Journal of the Royal Meteorological Society* 114(480): 373-398.

Clothier, B. E., K. L. Clawson, et al. (1986). "Estimation of soil heat flux from net radiation during the growth of alfalfa." *Agricultural and Forest Meteorology* 37(4): 319-329.

Crow, W. T. and W. P. Kustas (2005). "Utility of assimilating surface radiometric temperature observations for evaporative fraction and heat transfer coefficient retrieval." *Boundary-Layer Meteorology* 115(1): 105-130.

De Bruin, H. A. R. and A. A. M. Holtslag (1982). "A simple parameterization of the surface fluxes of sensible and latent heat during daytime compared with the Penman-Monteith concept." *Journal of Applied Meteorology* 21: 1610-1621.

Ekstrand, S. (1996). "Landsat TM-based forest damage assessment: correction for topographic effects." *Photogrammetric Engineering and Remote Sensing* 62(2): 151-161.

Gellens-Meulenberghs, F. (2005). "Sensitivity Tests of an Energy Balance Model to Choice of Stability Functions and Measurement Accuracy." *Boundary-Layer Meteorology* 115(3): 453-471.

Gillespie, A., S. Rokugawa, et al. (1998). "A temperature and emissivity separation algorithm for Advanced Spaceborne Thermal Emission and Reflection Radiometer (ASTER) images." *Geoscience and Remote Sensing, IEEE Transactions on* 36(4): 1113-1126.

Goutorbe, J. P. (1991). A critical assessment of the SAMER network accuracy. Land Surface Evaporation, Measurements and Parameterization, TJ Schmugge and J.-C. André, Eds, Springer-Verlag.

Gowda, P. H., J. L. Chavez, et al. (2008). "ET mapping for agricultural water management: present status and challenges." *Irrigation Science* 26(3): 223-237.

Gowda, P. H., J. L. Chávez, et al. (2007). "Remote sensing based energy balance algorithms for mapping ET: Current status and future challenges." *Transactions of the ASABE* 50(5): 1639-1644.

Grachev, A. A., C. W. Fairall, et al. (2000). "Convective profile constants revisited." *Boundary-Layer Meteorology* 94(3): 495-515.

Helder, D. (1999). "Radiometric characterization and calibration of Landsat 4/5 Thematic Mappers."

Helder, D., J. L. Barker, et al. (1996). Short term calibration of Landsat TM: Recent findings and suggested techniques, IEEE.

Helder, D., W. Boncyk, et al. (1997). "Landsat TM memory effect characterization and correction." *Canadian journal of remote sensing* 23(4): 299-308.

Hoëgström, U. L. F. (1988). "Non-dimensional wind and temperature profiles in the atmospheric surface layer: A re-evaluation." *Boundary-Layer Meteorology* 42(1): 55-78.

Jacob, F., A. Olioso, et al. (2002). "Mapping surface fluxes using airborne visible, near infrared, thermal infrared remote sensing data and a spatialized surface energy balance model." *Agronomie* 22(6): 669-680.

Jacob, F., F. Petitcolin, et al. (2004). "Comparison of land surface emissivity and radiometric temperature derived from MODIS and ASTER sensors." *Remote Sensing of Environment* 90(2): 137-152.

Kustas, W. P. and C. S. T. Daughtry (1990). "Estimation of the soil heat flux/net radiation ratio from spectral data." *Agricultural and Forest Meteorology* 49(3): 205-223.

Leblon, B., L. Gallant, et al. (1996). "Effects of shadowing types on ground-measured visible and near-infrared shadow reflectances." *Remote Sensing of Environment* 58(3): 322-328.

Levin, N., E. Ben-Dor, et al. (2004). "Topographic information of sand dunes as extracted from shading effects using Landsat images." *Remote Sensing of Environment* 90(2): 190-209.

Li, F., T. J. Jackson, et al. (2004). "Deriving land surface temperature from Landsat 5 and 7 during SMEX02/SMACEX." *Remote Sensing of Environment* 92(4): 521-534.

Li, X. and A. H. Strahler (1992). "Geometric-optical bidirectional reflectance modeling of the discrete crown vegetation canopy: Effect of crown shape and mutual shadowing." *Geoscience and Remote Sensing, IEEE Transactions on* 30(2): 276-292.

Mani, A., O. Chacko, et al. (1973). "Atmospheric turbidity over India from solar radiation measurements." *Solar Energy* 14(2): 185-195.

Marx, A., H. Kunstmann, et al. (2008). "Uncertainty analysis for satellite derived sensible heat fluxes and scintillometer measurements over Savannah environment and comparison to mesoscale meteorological simulation results." *Agricultural and Forest Meteorology* 148(4): 656-667.

Moran, M. S., R. D. Jackson, et al. (1995). "Reflectance factor retrieval from Landsat TM and SPOT HRV data for bright and dark targets." *Remote Sensing of Environment* 52(3): 218-230.

Nakai, T., A. Sumida, et al. (2008). "Parameterisation of aerodynamic roughness over boreal, cool-and warm-temperate forests." *Agricultural and Forest Meteorology* 148(12): 1916-1925.

Nerry, F., F. Petitcolin, et al. (1998). "Bidirectional Reflectivity in AVHRR Channel 3:: Application to a Region in Northern Africa." *Remote Sensing of Environment* 66(3): 298-316.

Oguntunde, P. G., A. E. Ajayi, et al. (2006). "Tillage and surface moisture effects on bare-soil albedo of a tropical loamy sand." *Soil and Tillage Research* 85(1-2): 107-114.

Petitcolin, F. and E. Vermote (2002). "Land surface reflectance, emissivity and temperature from MODIS middle and thermal infrared data." *Remote Sensing of Environment* 83(1-2): 112-134.

Raupach, M. R. (1992). "Drag and drag partition on rough surfaces." *Boundary-Layer Meteorology* 60(4): 375-395.

Raupach, M. R. (1994). "Simplified expressions for vegetation roughness length and zero-plane displacement as functions of canopy height and area index." *Boundary-Layer Meteorology* 71(1): 211-216.

Reginato, R. J., R. D. Jackson, et al. (1985). "Evapotranspiration calculated from remote multispectral and ground station meteorological data." *Remote Sensing of Environment* 18(1): 75-89.

Santos, C., I. J. Lorite, et al. (2008). "Integrating satellite-based evapotranspiration with simulation models for irrigation management at the scheme level." *Irrigation Science* 26(3): 277-288.

Schaepman-Strub, G., M. E. Schaepman, et al. (2006). "Reflectance quantities in optical remote sensing--definitions and case studies." *Remote Sensing of Environment* 103(1): 27-42.

Schaudt, K. J. and R. E. Dickinson (2000). "An approach to deriving roughness length and zero-plane displacement height from satellite data, prototyped with BOREAS data." *Agricultural and Forest Meteorology* 104(2): 143-155.

Sicart, J. E., R. Hock, et al. "Sky longwave radiation on tropical Andean glaciers: parameterization and sensitivity to atmospheric variables." *Journal of Glaciology* 56(199): 854-860.

Soil Survey Staff, Natural Resources Conservation Service, United States Department of Agriculture. Soil Survey Geographic (SSURGO) Database for [Survey Area, State]. Available online at <http://soildatamart.nrcs.usda.gov>.

Starks, P. J., J. M. Norman, et al. (1991). "Estimation of shortwave hemispherical reflectance (Albedo) from bidirectionally reflected radiance data." *Remote Sensing of Environment* 38(2): 123-134.

Stowe, L. L., A. Ignatov, et al. (1997). "Development, validation and potential enhancements to the second generation operational aerosol product at NOAA/NESDIS." *J. Geophys. Res* 102(16): 923–16.

Stricker, H. and W. Brutsaert (1978). "Actual evapotranspiration over a summer period in the." *Journal of Hydrology* 39(1-2): 139-157.

Tang, Q., S. Peterson, et al. (2009). "Satellite-based near-real-time estimation of irrigated crop water consumption." *Journal of geophysical research* 114(D5): D05114.

Tasumi, M. (2003). "Progress in operational estimation of regional evapotranspiration using satellite imagery."

Tasumi, M., R. G. Allen, et al. (2008). "At-surface reflectance and albedo from satellite for operational calculation of land surface energy balance." *Journal of Hydrologic Engineering* 13: 51.

Teillet, P. M., J. L. Barker, et al. (2001). "Radiometric cross-calibration of the Landsat-7 ETM+ and Landsat-5 TM sensors based on tandem data sets." *Remote Sensing of Environment* 78(1-2): 39-54.

Tian, X., Z. Y. Li, et al. "Estimating zero-plane displacement height and aerodynamic roughness length using synthesis of LiDAR and SPOT-5 data." *Remote Sensing of Environment* 115(9): 2330-2341.

Van der Kwast, J., W. Timmermans, et al. (2009). "Evaluation of the Surface Energy Balance System (SEBS) applied to ASTER imagery with flux-measurements at the SPARC 2004 site (Barrax, Spain)." *Hydrol. Earth Syst. Sci* 13: 1337-1347.

Verhoef, A., K. G. McNaughton, et al. (1997). "A parameterization of momentum roughness length and displacement height for a wide range of canopy densities." *Hydrology and Earth System Sciences* 1(1): 81-91.

Vogelmann, J. E., D. Helder, et al. (2001). "Effects of Landsat 5 Thematic Mapper and Landsat 7 Enhanced Thematic Mapper Plus radiometric and geometric calibrations and corrections on landscape characterization* 1." *Remote Sensing of Environment* 78(1-2): 55-70.

Wall, G. W. and E. T. Kanemasu (1990). "Carbon dioxide exchange rates in wheat canopies. Part I. Influence of canopy geometry on trends in leaf area index, light interception and instantaneous exchange rates." *Agricultural and Forest Meteorology* 49(2): 81-102.

Walter, I. A., R. G. Allen, et al. (2000). ASCE's standardized reference evapotranspiration equation.

Wang, J., T. W. Sammis, et al. (2009). "Sensitivity Analysis of the Surface Energy Balance Algorithm for Land (SEBAL)." *Transactions of the ASABE* 52(3): 801-811.

Wang, J., Y. Ma, et al. (1995). "The scaling-up of processes in the heterogeneous landscape of HEIFE with the aid of satellite remote sensing: HEIFE." *Journal of the Meteorological Society of Japan* 73(6): 1235-1244.

Watts, C. J., A. Chehbouni, et al. (2000). "Comparison of sensible heat flux estimates using AVHRR with scintillometer measurements over semi-arid grassland in northwest Mexico." *Agricultural and Forest Meteorology* 105(1-3): 81-89.

Wukelic, G. E., D. E. Gibbons, et al. (1989). "Radiometric calibration of Landsat Thematic Mapper thermal band." *Remote Sensing of Environment* 28: 339-347.

Wulf, O. R. (1930). "The Band Spectrum of Ozone in the Visible and Photographic Infra-Red." *Proceedings of the National Academy of Sciences of the United States of America* 16(7): 507.

Xu, W., M. J. Wooster, et al. (2008). "Modelling of urban sensible heat flux at multiple spatial scales: A demonstration using airborne hyperspectral imagery of Shanghai and a temperature-emissivity separation approach." *Remote Sensing of Environment* 112(9): 3493-3510.

Yang, K., T. Koike, et al. (2006). "Improving estimation of hourly, daily, and monthly solar radiation by importing global data sets." *Agricultural and forest meteorology* 137(1-2): 43-55.

Appendix A: Variations in calibration coefficients a,b when transmissivity is changed. These two complement each other to adjust sensible heat flux H, to match output ET with the weather station's ET.

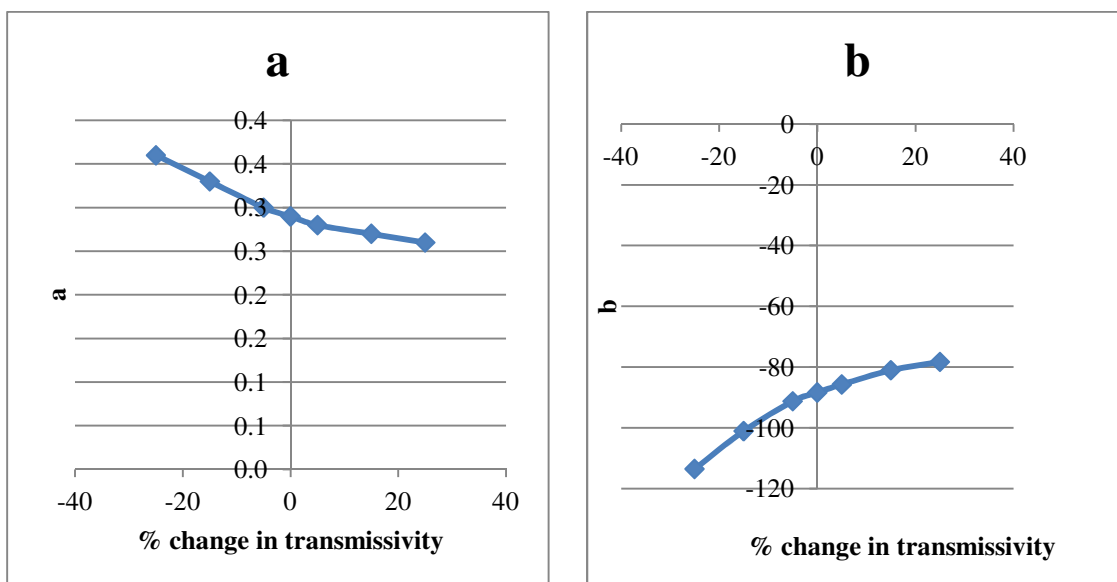


Figure A.1 Variations in a,b with change in Transmissivity for May image

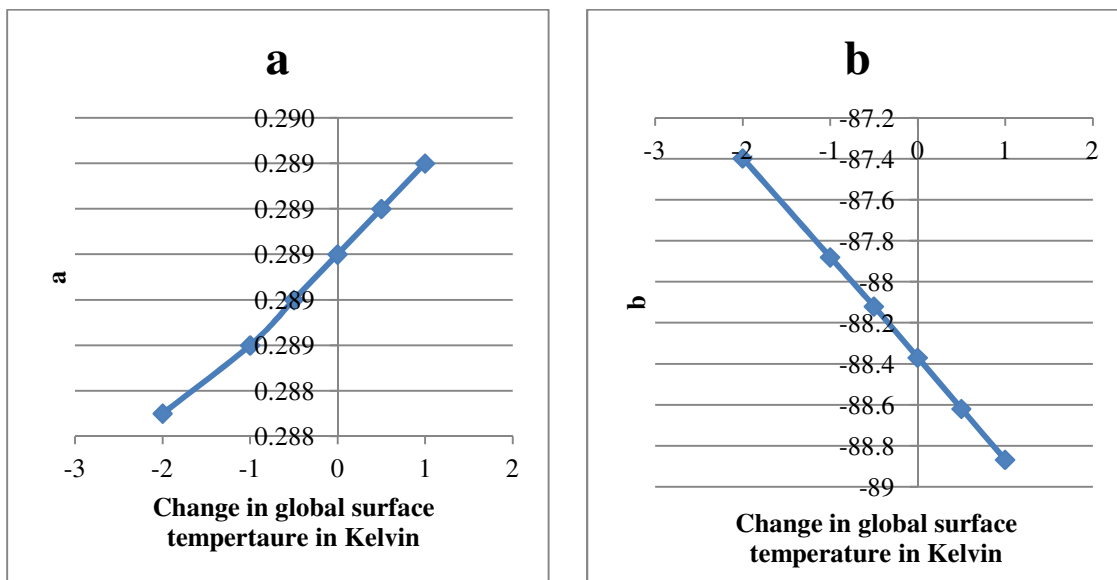


Figure A.2 Variations in a,b with change in ET_r for May image